Multimode Jahn−Teller and Pseudo-Jahn−Teller Interactions in the Cyclopropane Radical Cation: Complex Vibronic Spectra and Nonradiative Decay Dynamics

5 AUTHORS, INCLUDING:

Susanta Mahapatra
University of Hyderabad
114 PUBLICATIONS   1,626 CITATIONS

SEE PROFILE

Hans-Dieter Meyer
Universität Heidelberg
245 PUBLICATIONS   9,779 CITATIONS

SEE PROFILE

Horst Köppel
Universität Heidelberg
240 PUBLICATIONS   5,937 CITATIONS

SEE PROFILE

Multimode Jahn−Teller and Pseudo-Jahn−Teller Interactions in the Cyclopropane Radical Cation: Complex Vibronic Spectra and Nonradiative Decay Dynamics

T. S. Venkatesan and S. Mahapatra*

School of Chemistry, University of Hyderabad, Hyderabad 500 046, India

H.-D. Meyer, H. Köppel,* and L. S. Cederbaum

Theoretical Chemistry, Institute of Physical Chemistry, University of Heidelberg, Im Neuenheimer Feld 229, D-69120 Heidelberg, Germany

The complex vibronic spectra and the nonradiative decay dynamics of the cyclopropane radical cation (CP^+) are simulated theoretically with the aid of a time-dependent wave packet propagation approach using the multireference time-dependent Hartree scheme. The theoretical results are compared with the experimental photoelectron spectrum of cyclopropane. The ground and first excited electronic states of CP^+ are of $\tilde{X}^2E'$ and $\tilde{A}^2E''$ type, respectively. Each of these degenerate electronic states undergoes Jahn−Teller (JT) splitting when the radical cation is distorted along the degenerate vibrational modes of e′ symmetry. The JT split components of these two electronic states can also undergo pseudo-Jahn−Teller (PJT)-type crossings via the vibrational modes of e″, a_1'' and a_2'' symmetries. These lead to the possibility of multiple multidimensional conical intersections and highly nonadiabatic nuclear motions in these coupled manifolds of electronic states. In a previous publication [*J. Phys. Chem. A* **2004,** *108,* 2256], we investigated the JT interactions alone in the $\tilde{X}^2E'$ ground electronic manifold of CP^+. In the present work, the JT interactions in the $\tilde{A}^2E''$ electronic manifold are treated, and our previous work is extended by considering the coupling between the $\tilde{X}^2E'$ and $\tilde{A}^2E''$ electronic states of CP^+. The nuclear dynamics in this coupled manifold of two JT split doubly degenerate electronic states is simulated by considering fourteen active and most relevant vibrational degrees of freedom. The vibronic level spectra and the ultrafast nonradiative decay of the excited cationic states are examined and are related to the highly complex entanglement of electronic and nuclear degrees of freedom in this prototypical molecular system.

I. Introduction

The Jahn−Teller (JT) effect[1−5] represents an important vibronic coupling mechanism for a nonlinear molecule in a degenerate electronic state. Upon distortion along suitable vibrational modes, the orbital degeneracy is lifted and as a result the symmetry of the system breaks and it moves to a configuration of lower symmetry. The JT split electronic states form conical intersections[6−11] at the equilibrium geometry of the undistorted configuration, and therefore cause nonadiabatic transitions during nuclear vibrations of the molecule. Depending on the strength of the nonadiabatic coupling of the associated electronic states, the vibronic energy level spectrum of the system reveals a complex pattern. A theoretical simulation of such spectrum requires us to go beyond the well-known Born−Oppenheimer (BO) description of the electronic and nuclear motion in a molecular system.[12−14] Symmetry allowed interactions between a degenerate and a nondegenerate or two degenerate electronic states are also possible and these are known as pseudo-Jahn−Teller (PJT)-type interactions.[5−7,15−17] Although the PJT interactions of the former type are well studied in the literature, not much is known about the latter type. In this Article, we consider the PJT interactions of the latter type, occurring between two low-lying JT split doubly degenerate

* To whom correspondence should be addressed: E-mail: smsc@ uohyd.ernet.in (S.M.), Horst.Koeppel@pci.uni-heidelberg.de (H.K.).

electronic states of the prototypical cyclopropane radical cation (CP^+), and attempt to develop a vibronic coupling model to unravel the complex features observed in its vibronic energy level spectrum.

The equilibrium configuration of the cyclopropane (CP) molecule belongs to the D_{3h} symmetry point group. Ionization of an electron from its two highest occupied 3e′ and 1e″ molecular orbitals forms CP^+ in the ground $\tilde{X}^2E'$ and first excited $\tilde{A}^2E''$ electronic states, respectively. The 21 vibrational degrees of freedom of CP are grouped into $3a_1'$, a_2', 4e′, a_1'', $2a_2''$, and 3e″ irreducible representations of the D_{3h} symmetry point group. The symmetrized direct product of two E′ or E″ representations in the D_{3h} point group yields

$$(E')^2 = (E'')^2 = a_1' + e' \tag{1}$$

Similarly, the direct product of E′ and E″ irreducible representations in the D_{3h} symmetry point group yields

$$E' \times E'' = a_1'' + a_2'' + e'' \tag{2}$$

The above elementary symmetry selection rules (eqs 1−2) suggest that the degenerate $\tilde{X}^2E'$ and $\tilde{A}^2E''$ electronic states of CP^+ would undergo JT splitting in first order when distorted along the degenerate vibrational modes of e′ symmetry. These two degenerate electronic states may also undergo PJT-type interactions along the vibrational modes of a_1'', a_2'', and e″
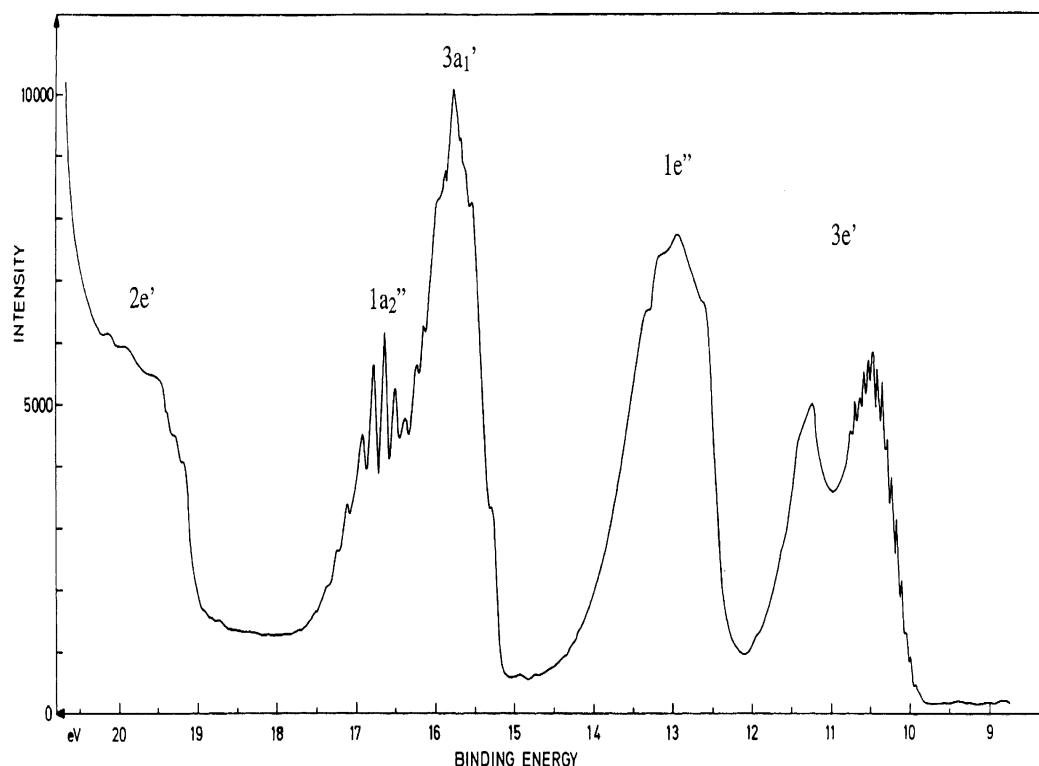
Figure 1. He I experimental photoelectron spectrum of cyclopropane reproduced from ref 20.

symmetries. Although these two degenerate electronic states are separated by ∼2.428 eV in energy at the equilibrium configuration of neutral CP, such interactions are found to be important in the energy range of its photoelectron bands considered in this article. The PJT coupling of two JT split degenerate electronic states is expected to yield a series of conical intersections and consequently the nuclear motion may become highly nonadiabatic owing to the possibility of nonradiative transitions to four component electronic states.

The photoelectron spectrum of CP has been recorded by various experimental groups.[18−26] Among these, the recent 21.22 eV recording of Holland et al.[20] using synchrotron and He I radiation as ionization sources seems to be better resolved. The photoelectron band recorded by these authors in the 9−20 eV electron binding energy range is reproduced from ref 20 in Figure 1. It exhibits a twin band centered around ∼11 eV, a broad band at ∼13.2 eV, and two strongly overlapping bands at ∼15.7 and ∼16.5 eV. These bands emerge from the ionization of an electron from the 3e′, 1e″, 3a₁′ and 1a₂″ molecular orbitals of CP, respectively. Among them, the first two bands are of special interest and are considered here. They represent the vibronic structures of the JT split $\tilde{X}^2E'$ and $\tilde{A}^2E''$ electronic states of CP$^+$. The second band, in particular, exhibits a highly diffuse pattern and is structureless. This indicates that underlying nuclear motion in the $\tilde{A}^2E''$ electronic manifold is strongly perturbed by complex vibronic interactions. Unraveling of this issue is one of the main objectives of the present investigation.

To examine the JT and PJT coupling effects on the nuclear dynamics in the two low-lying degenerate electronic states of CP$^+$, we have undertaken a detailed ab initio dynamical study of the photoionization spectrum of CP (cf. Figure 1). In a previous publication,[27] we have treated the JT interactions in the $\tilde{X}^2E'$ electronic manifold of CP$^+$ by constructing a two-states and eleven-modes model vibronic Hamiltonian within a quadratic vibronic coupling scheme by an ab initio quantum dynamical approach. Our results were shown to compare well with the high-resolution He I excited recording of Holland and

co-workers[20] (cf. Figure 1). The strong JT interactions within this state lead to the observed bimodal intensity distribution of the first photoelectron band. The separation between the two maxima of the bimodal profile of ∼0.80 eV was in good agreement with the experimental value of ∼0.78 eV. Two Condon active (a₁′) and three JT active (e′) vibrational modes were found to contribute mostly to the nuclear dynamics in this electronic manifold.[27]

The highly diffuse nature and the absence of a bimodal intensity distribution of the second photoelectron band indicates that the JT effect in the $\tilde{A}^2E''$ electronic manifold is not as strong as that in the $\tilde{X}^2E'$ ground electronic manifold. However, the $\tilde{X}-\tilde{A}$ PJT interactions seem to be particularly important for the detailed vibronic structure of this band. Our analysis reveals significant PJT coupling due to the a₁″ and one of the three e″ vibrational modes. Therefore, in this work we attempt to develop a theoretical model to describe this $\tilde{X}-\tilde{A}$ PJT interactions (including the JT interactions) of these two degenerate electronic states. The present work therefore represents a rigorous extension of our earlier theoretical model developed to treat the JT interactions in the $\tilde{X}^2E'$ electronic manifold alone. In what follows, a quadratic coupling scheme is employed for the JT active e′ vibrational modes and the Condon active a₁′ vibrational modes, whereas the PJT active a₁″ and e″ vibrational modes are treated within a linear coupling scheme. Therefore, the complete theoretical model developed here consists of four interacting electronic states and fourteen nuclear degrees of freedom. We mention that vibronic coupling in CP$^+$ represents a unique example in which degenerate vibrational modes of two different symmetries are involved in the JT and PJT activities.

Detailed ab initio electronic structure calculations are carried out to derive the relevant coupling parameters of the vibronic Hamiltonian. A time-independent matrix diagonalization approach to treat the nuclear dynamics on four interacting electronic states including fourteen vibrational degrees of freedom is computationally impracticable. This task is therefore accomplished with a time-dependent wave packet (WP) propa-

gation approach within the multiconfiguration time-dependent Hartree (MCTDH) scheme.[28−30] The MCTDH scheme has been very successful particularly in treating the multistate and multimode vibronic coupling problems of large dimensions. The details of the MCTDH method is documented in a recent review article by Beck et al.[31] In the recent past, this method has been successfully applied to treat very complex vibronic coupling in $C_6H_6^{+}$ [32] and $C_5H_4^{+}$.[33] The final results of this paper are obtained by this method, and comparison calculations are carried out in reduced dimensions by the time-independent matrix diagonalization approach, to check the consistencies of various results and also to examine the detailed vibrational progressions in the photoelectron bands. A systematic treatment of the nuclear dynamics revealed that PJT interactions between the $\tilde{X}^2E'$ and $\tilde{A}^2E''$ electronic states of CP^+ play an important role in the detailed structure of the photoelectron bands. The minimum of the seam of PJT conical intersections is found to occur ∼1.475 eV above and ∼0.638 eV below the minimum of the JT conical intersections of the $\tilde{X}^2E'$ and $\tilde{A}^2E''$ electronic states, respectively. The PJT couplings due to a_1'' and e'' vibrational modes cause a huge increase in the spectral line density and as a result second maxima of the first photoelectron band and the entire second photoelectron band, exhibit a structureless pattern, despite the JT effect in the $\tilde{A}^2E''$ electronic manifold is weaker compared to that in the $\tilde{X}^2E'$ electronic manifold. The theoretical results are found to be in excellent agreement with the experimental data.

In the following, the construction of the vibronic Hamiltonian and the principles of calculation of the photoelectron spectrum are described in section II. The numerical calculation of the latter by time-independent and time-dependent quantum mechanical approaches is outlined in section III. The details of the electronic structure and the stationary observables like vibronic level spectra, and time-dependent observables like electronic populations and the motion of the WP in the coupled manifold of electronic states, are presented and discussed in section IV. Finally, the content of the paper is summarized in section V.

II. Theoretical Approach

A. Vibronic Hamiltonian. The photoionization to the two low-lying degenerate $\tilde{X}^2E'$ and $\tilde{A}^2E''$ electronic states of CP^+ is theoretically examined here. As stated in the Introduction, each of these two electronic states undergo JT splitting when CP^+ is perturbed along the degenerate vibrational modes of e' symmetry. The symmetry selection rule (eq 2) allows the JT split component states of the two degenerate electronic states to exhibit PJT-type interactions via the vibrational modes of a_1'' and e'' symmetries. In addition, there are three totally symmetric a_1' vibrational modes that are Condon active in each of these two electronic states. In the following, we first resort to a diabatic electronic basis[34] to treat this vibronic coupling problem. This is to avoid the numerical difficulties[7] that arise due to the singular nature of the nonadiabatic coupling terms in an adiabatic electronic basis. The diabatic vibronic Hamiltonian is constructed in terms of the dimensionless normal coordinates of the electronic ground state of neutral CP. To a good approximation the vibrational motion in the latter is treated as harmonic. In the following, we refer to Q_i as the dimensionless normal coordinate of the vibrational mode ν_i with a harmonic vibrational frequency ω_i. Actually, each Q_i represents the normal displacement coordinate from the equilibrium configuration of electronic ground state of CP at $\mathbf{Q} = 0$. In the rest of the paper

the three a_1' vibrational modes are numbered as ν_1, ν_2, and ν_3, the four e' vibrational modes as ν_4, ν_5, ν_6, and ν_7, and one a_1'' and one of the three e'' vibrational modes as ν_8 and ν_9, respectively. Following the well-known vibronic coupling theory,[7] we represent the diabatic vibronic Hamiltonian of the coupled manifold of four interacting electronic states as

$$\mathcal{H} = \mathcal{H}_0 \mathbf{1_4} + \begin{pmatrix} a_{11} & a_{12} & a_{13} & a_{14} \\ & a_{22} & a_{23} & a_{24} \\ \text{h.c.} & & a_{33} & a_{34} \\ & & & a_{44} \end{pmatrix} \quad (3)$$

Here $\mathcal{H}_0 = \mathcal{T}_N + \mathcal{V}_0$, with

$$\mathcal{T}_N = -\frac{1}{2}\sum_{i=1}^{3}\omega_i\frac{\partial^2}{\partial Q_i^2} - \frac{1}{2}\sum_{i=4}^{7}\omega_i\left(\frac{\partial^2}{\partial Q_{xi}^2} + \frac{\partial^2}{\partial Q_{yi}^2}\right) - \frac{1}{2}\omega_8\frac{\partial^2}{\partial Q_8^2} - \frac{1}{2}\omega_9\left(\frac{\partial^2}{\partial Q_{x9}^2} + \frac{\partial^2}{\partial Q_{y9}^2}\right) \quad (4)$$

and

$$\mathcal{V}_0 = \frac{1}{2}\sum_{i=1}^{3}\omega_i Q_i^2 + \frac{1}{2}\sum_{i=4}^{7}\omega_i(Q_{xi}^2 + Q_{yi}^2) + \frac{1}{2}\omega_8 Q_8^2 + \frac{1}{2}\omega_9(Q_{x9}^2 + Q_{y9}^2) \quad (5)$$

is the Hamiltonian matrix associated with the ground electronic state of CP and is defined in terms of unperturbed harmonic oscillators with frequencies ω_i. The matrix Hamiltonian with elements a_{ij} in eq 3 describes the change in the electronic energy upon ionization from the electronic ground state of CP. These elements are expanded in a Taylor series around the D_{3h} equilibrium geometry of CP along each of the normal mode displacement coordinates. The series is truncated after the second-order terms for the symmetric a_1' and JT active e' vibrational modes, whereas up to the first-order terms are retained only for the PJT active a_1'' and e'' modes. Excluding the various bilinear coupling terms, the following results are obtained in conjunction with the elementary symmetry selection rules (as stated above) and a rigorous group theoretical analysis (given in the appendix):[7]

$$a_{11} = E_{E'}^0 + \sum_{i=1}^{3}\kappa_i' Q_i + \sum_{i=4}^{7}\lambda_i' Q_{xi} + \frac{1}{2}\sum_{i=1}^{3}\gamma_i' Q_i^2 + \frac{1}{2}\sum_{i=4}^{7}[\gamma_i'(Q_{xi}^2 + Q_{yi}^2) + \eta_i'(Q_{xi}^2 - Q_{yi}^2)] \quad (6a)$$

$$a_{22} = E_{E'}^0 + \sum_{i=1}^{3}\kappa_i' Q_i - \sum_{i=4}^{7}\lambda_i' Q_{xi} + \frac{1}{2}\sum_{i=1}^{3}\gamma_i' Q_i^2 + \frac{1}{2}\sum_{i=4}^{7}[\gamma_i'(Q_{xi}^2 + Q_{yi}^2) - \eta_i'(Q_{xi}^2 - Q_{yi}^2)] \quad (6b)$$

$$a_{33} = E_{E''}^0 + \sum_{i=1}^{3}\kappa_i'' Q_i + \sum_{i=4}^{7}\lambda_i'' Q_{xi} + \frac{1}{2}\sum_{i=1}^{3}\gamma_i'' Q_i^2 + \frac{1}{2}\sum_{i=4}^{7}[\gamma_i''(Q_{xi}^2 + Q_{yi}^2) + \eta_i''(Q_{xi}^2 - Q_{yi}^2)] \quad (6c)$$

Jahn−Teller Interactions in Cyclopropane Radical Cation

J. Phys. Chem. A, Vol. 111, No. 10, 2007 **1749**

$$a_{44} = E_{E''}^0 + \sum_{i=1}^{3} \kappa_i'' Q_i - \sum_{i=4}^{7} \lambda_i'' Q_{xi} + \frac{1}{2}\sum_{i=1}^{3} \gamma_i'' Q_i^2 +$$
$$\frac{1}{2}\sum_{i=4}^{7} [\gamma_i''(Q_{xi}^2 + Q_{yi}^2) + \eta_i''(Q_{xi}^2 - Q_{yi}^2)] \quad (6d)$$

$$a_{12} = \sum_{i=4}^{7} (\lambda_i' Q_{yi} - \eta_i' Q_{xi} Q_{yi}) \quad (6e)$$

$$a_{13} = \lambda_9 Q_{x9} \quad (6f)$$

$$a_{14} = \lambda_8 Q_8 + \lambda_9 Q_{y9} \quad (6g)$$

$$a_{23} = -\lambda_8 Q_8 + \lambda_9 Q_{y9} \quad (6h)$$

$$a_{24} = -\lambda_9 Q_{x9} \quad (6i)$$

$$a_{34} = \sum_{i=4}^{7} (\lambda_i'' Q_{yi} - \eta_i'' Q_{xi} Q_{yi}) \quad (6j)$$

Here $E_{E'}^0$ and $E_{E''}^0$ are the vertical ionization potentials of the $\tilde{X}^2E'$ and $\tilde{A}^2E''$ electronic states of CP$^+$, respectively. The quantities κ_i' and κ_i'' are the linear intrastate coupling constants for the totally symmetric vibrational modes ($i = 1-3$). The parameters λ_i' and λ_i'' are the linear JT coupling constants for the JT active degenerate vibrational modes ($i = 4-7$). The quantities γ_i' and γ_i'' denote the diagonal second-order coupling parameters for the vibrational modes, $i = 1-7$, whereas η_i' and η_i'' denote the quadratic JT coupling parameters for the vibrational modes, $i = 4-7$. The primed and doubly primed parameters are associated with the $\tilde{X}^2E'$ and $\tilde{A}^2E''$ electronic states, respectively. The linear PJT coupling parameters for the a_1'' and e'' vibrational modes are designated as λ_8 and λ_9, respectively. The calculations of these parameters are discussed in section IV.A below, and their numerical values are given in Table 1.

B. Photoelectron Spectrum. The photoelectron spectrum is calculated by using Fermi's golden rule. According to this rule, the spectral intensity is given by

$$P(E) = \sum_{v} |\langle\Psi_v|\hat{T}|\Psi_0\rangle|^2 \delta(E - E_v + E_0) \quad (7)$$

Here, $|\Psi_v\rangle$ represents the final coupled $\tilde{X}E'-\tilde{A}^2E''$ vibronic states of CP$^+$ and E_v is the vibronic energy (eigenenergy of the Hamiltonian (eqs 3−6j)). $|\Psi_0\rangle$ is the initial electronic and vibrational ground state of neutral CP with energy E_0. The quantity $\hat{T}$ is the transition operator that describes the interaction of the $3e'$ and $1e''$ valence electrons of CP$^+$ with the external electromagnetic radiation. The quantity E is the difference of energy of the external radiation and the kinetic energy of the ejected electron and therefore represents the electron binding energy or the ionization energy. The initial and the final electronic states can be expressed as follows:

$$|\Psi_0\rangle = |\Phi^0\rangle|\chi_0^0\rangle \quad (8)$$

$$|\Psi_v\rangle = |\Phi^{E_x'}\rangle|\chi_v^{E_x'}\rangle + |\Phi^{E_y'}\rangle|\chi_v^{E_y'}\rangle + |\Phi^{E_x''}\rangle|\chi_v^{E_x''}\rangle +$$
$$|\Phi^{E_y''}\rangle|\chi_v^{E_y''}\rangle \quad (9)$$

where $|\Phi\rangle$ and $|\chi\rangle$ represent the diabatic electronic and vibrational part of the wavefunction, respectively. The super-

scripts 0, E$_x'$/E$_y'$ and E$_x''$/E$_y''$ refer to the $\tilde{X}^1A_1'$ electronic ground state of CP, the x/y components of the E$'$ electronic state, and the x/y components of the E$''$ electronic state of CP$^+$, respectively. Using eqs 8 and 9, the excitation function of eq 7 can be rewritten as

$$P(E) = \sum_{v} |\tau^{E_x'}\langle\chi_v^{E_x'}|\chi_0^0\rangle + \tau^{E_y'}\langle\chi_v^{E_y'}|\chi_0^0\rangle + \tau^{E_x''}\langle\chi_v^{E_x''}|\chi_0^0\rangle +$$
$$\tau^{E_y''}\langle\chi_v^{E_y''}|\chi_0^0\rangle|^2 \delta(E - E_v + E_0) \quad (10)$$

where

$$\tau^m = \langle\Phi^m|\hat{T}|\Phi^0\rangle \quad (11)$$

represents the matrix elements of the transition dipole operator of the final $\tilde{X}E'-\tilde{A}^2E''$ coupled electronic states of CP$^+$. In rewriting eq 10, the matrix elements of the transition dipole operator are treated to be independent of nuclear coordinates. These elements are not calculated in the present study and are treated as constants, in accordance with the applicability of the generalized Condon approximation in a diabatic electronic basis.[35]

In a time-dependent picture, the Fourier transform representation of the delta function is used in the above golden rule formula. The resulting expression for the spectral intensity then rearranges to the Fourier transform of the time autocorrelation function of the wave packet[32]

$$P(E) \sim 2\text{Re} \int_0^\infty e^{iEt/\hbar}\langle 0|\boldsymbol{\tau}^\dagger e^{-i\mathscr{H}t/\hbar}\boldsymbol{\tau}|0\rangle \, dt \quad (12)$$

$$\sim 2\text{Re} \int_0^\infty e^{iEt/\hbar} C^m(t) \, dt \quad (13)$$

The quantity $C^m(t) = \langle\Psi_m(0)|\Psi_m(t)\rangle$ is the time autocorrelation function of the wave packet initially prepared on mth electronic state. $\boldsymbol{\tau}$ refers to the transition dipole matrix; $\boldsymbol{\tau}^\dagger = (\tau^{E_x'}, \tau^{E_y'}, \tau^{E_x''}, \tau^{E_y''})$ with τ^m given by eq 11 and, $\Psi_m(t) = e^{-i\mathscr{H}t/\hbar}\tau^m|0\rangle$. Note that Ψ possesses components on each of the vibronically coupled four diabatic electronic states (E$_x'$, E$_y'$, E$_x''$, and E$_y''$), and therefore the composite photoelectron spectrum is written as a sum of the resulting four partial spectra, calculated by propagating wave packets for four different initial conditions. Finally, in eq 13 use is made of a vibronic symmetry, whereby only terms $|\tau^m|^2$ contribute to the spectrum and the mixed terms $\tau^m\tau^{n*}$, still present in eq 10, vanish.[7]

III. Numerical Simulations

A. Time-Independent Approach. The eigenvalue spectrum of the four-state (or 4×4) matrix Hamiltonian $\mathscr{H}$ of eq 3 are calculated by a numerically exact solution of the time-independent Schrödinger equation

$$\mathscr{H}|\Psi_v\rangle = E_v|\Psi_v\rangle \quad (14)$$

In this approach, the vibronic states $|\Psi_v\rangle$ are represented as a complete direct product basis of diabatic electronic states Φ^m and one-dimensional harmonic oscillator eigenfunctions $|v_i\rangle$ of $\mathscr{H}_0$. The vibronic Hamiltonian expressed in this basis becomes a function of the occupation number of the various vibrational modes. The maximum level of excitation for each mode is approximately estimated from the corresponding Poisson parameter $[(^1/_2)[(\kappa \text{ or } \lambda)/\omega]^2]$. The Hamiltonian matrix written in such a direct product basis is usually highly sparse and is tridiagonalized using the Lanczos algorithm prior to diagonalization.[36] The diagonal elements of the resulting eigenvalue matrix give the eigenenergies of the vibronic energy levels, and the relative intensities of the vibronic lines are calculated from

TABLE 1: Ab Initio Calculated Linear and Quadratic Coupling Constants for the X̃²E′ and Ã²E″ Electronic States of CP⁺ ᵃ

mode (symmetry)	κ_i' or λ_i' X̃²E′	κ_i'' or λ_i'' Ã²E″	γ_i' X̃²E′	γ_i'' Ã²E″	η_i' X̃²E′	η_i'' Ã²E″	MP2/cc-pVTZ X̃²E′ ⊗ Ã²E″ ω_i	λ_i
ν_1 (a$_1'$)	−0.109 (0.254)	−0.012 (0.003)	-1.902×10^{-3} ᵇ	-1.092×10^{-2}			0.1531	
ν_2 (a$_1'$)	0.214 (0.635)	−0.298 (1.228)	4.350×10^{-3} ᵇ	-6.176×10^{-2}			0.1902	
ν_3 (a$_1'$)	0.018 (0.001)	0.324 (0.333)	1.324×10^{-3} ᵇ	1.635×10^{-2}			0.3965	
ν_4 (e′)	0.320 (4.019)	0.138 (0.743)	1.442×10^{-3}	-6.685×10^{-3}	-3.772×10^{-3} ᵇ	-2.494×10^{-3}	0.1129	
ν_5 (e′)	0.370 (3.997)	0.041 (0.050)	5.784×10^{-3}	-7.716×10^{-2}	-7.410×10^{-3} ᵇ	-8.052×10^{-3}	0.1309	
ν_6 (e′)	0.069 (0.071)	0.224 (0.741)	-6.586×10^{-3}	-9.558×10^{-2}	-3.648×10^{-3} ᵇ	3.456×10^{-2}	0.1841	
ν_7 (e′)	0.033 (0.003)	0.233 (0.174)	2.441×10^{-3}	-6.858×10^{-3}	6.692×10^{-4} ᵇ	8.833×10^{-3}	0.3954	
ν_8 (a$_1'$)							0.1449	0.3280
ν_9 (e″)							0.1514	0.1836
$E_{E'}^0$	10.801							
$E_{E''}^0$	13.229							

ᵃ The vertical ionization energies of these two electronic states and the harmonic vibrational frequencies of the electronic ground state of CP are also given in the table. All quantities are in eV. The dimensionless Poisson parameters $(\kappa_i'/\omega_i)^2/2$, $(\lambda_i'/\omega_i)^2/2$, $(\kappa_i''/\omega_i)^2/2$, and $(\lambda_i''/\omega_i)^2/2$ are given in parentheses. ᵇ There was a typographical error for these numbers in Table 2 of ref 27. The values reported there were a factor of 2 smaller than the present values.

the squared first components of the Lanczos eigenvectors.[36,37] Further details of this numerical approach can be found in ref 7.

B. Time-Dependent Approach. In this approach, the eigenvalue spectrum of the vibronic Hamiltonian is calculated by numerically solving the time-dependent Schrödinger (TDSE) equation

$$i\hbar \frac{\partial |\Psi\rangle}{\partial t} = \mathscr{H}|\Psi\rangle \qquad (15)$$

using the MCTDH scheme. The latter provides an efficient algorithm in propagating the wave packets rather effectively with much less computational overheads. Because the details of this method have been extensively discussed in the literature,[29−31] we highlight only the essentials here. The basis of the method is to use a multiconfigurational ansatz (product separable) for the wave function, with each configuration being expressed as a Hartree product of time-dependent basis functions, known as single particle functions (SPFs). For the nonadiabatic problem examined here, a *multiset* formulation is much more appropriate and the corresponding wave function can be expanded as

$$\Psi(Q_1,Q_2,...,Q_f,t) = \Psi(q_1,q_2,...,q_p,t)$$

$$= \sum_{\alpha=1}^{4} \sum_{j_1=1}^{n_1^{(\alpha)}} \cdots \sum_{j_p=1}^{n_p^{(\alpha)}} A_{j_1 \cdots j_p}^{(\alpha)}(t) \prod_{k=1}^{p} \phi_{j_k}^{(\alpha,k)}(q_k,t)|\alpha\rangle \qquad (16)$$

$$= \sum_{\alpha} \sum_{J} A_J^{(\alpha)} \Phi_J^{(\alpha)}|\alpha\rangle \qquad (17)$$

where f and p represent the number of vibrational degrees of freedom, and MCTDH *particles* (also called *combined* modes), respectively. $A_{j_1 \cdots j_p}^{(\alpha)}$ denote the MCTDH expansion coefficients and the $\phi_{j_k}^{(\alpha,k)}$ are the one-dimensional expansion functions, known as SPFs. The labels $\{\alpha\}$ are indices denoting the discrete set of electronic states considered in the calculation. Thus, the WP, $\Psi^{(\alpha)}$ $(=\sum_J A_J^{(\alpha)} \Phi_J^{(\alpha)})$ associated with each electronic state is described using a different set of SPFs, $\{\phi_{j_k}^{(\alpha,k)}\}$. Here the multiindex $J = j_1, ..., j_p$ depends implicitly on the state α as the maximum number of SPFs may differ for different states. The summation $\sum_J$ is a shorthand notation for summation over all possible index combinations for the relevant electronic state.

The variables for the p sets of SPFs are defined in terms of one or multidimensional coordinates of a particle.

The equations of motion for the expansion coefficients, $A_J^{(\alpha)}$, and SPFs, $\phi_{j_k}^{(\alpha,k)}$, have been derived using the Dirac−Frankel variational principle.[38,39] The resulting equations of motion are coupled differential equations for the coefficients and the SPFs. For k degrees of freedom there are n_k SPFs, and these SPFs are represented by N_k primitive basis functions or grid points. The efficiency of the MCTDH algorithm grows with increasing N_k/n_k.[31] The use of the variational principle ensures that the SPFs evolve so as to optimally describe the true WP; i.e., the time-dependent basis moves with the WP. This provides the efficiency of the method by keeping the basis optimally small.

In general, for nonadiabatic problems of the present type, MCTDH is quite capable of handling 20−30 vibrational degrees of freedom. CP has 21 vibrational degrees of freedom (seven nondegenerate and seven doubly degenerate), and we find that only 14 of them are relevant and need to be considered in the nuclear dynamics treated here. So, the physical system is described by a set of $f = 14$ coordinates, $Q_1, ..., Q_f$. For large systems, let us say, for $f \geq 6$, it is important to combine degrees of freedom to make the calculation computationally feasible. The collection of combined degrees of freedom is called a particle.[31] Thus, a particle coordinate is chosen to be a set of coordinates: i.e., $q_k = [Q_1, Q_2, ...]$. The SPFs are then multidimensional functions of the set of system coordinates and the number of particles $p < f$. By doing so, the computational resources can be significantly reduced and high-dimensional systems can be treated without affecting the variational nature of the method. However, the multimode problems remain an open challenge because the exponential growth in the computational resources restricts a calculation to below 6−8 particles.

To set up an MCTDH calculation, one needs to choose a set of primitive basis functions in the first step. The SPFs, their time derivatives and the Hamiltonian are then represented in this basis at each point in time. A combination scheme for the degrees of freedom is then selected to reduce the computational requirements and finally, a set of SPFs is specified to accurately represent the evolving WP. The primitive basis chosen is a harmonic oscillator discrete variable representation (DVR). The initial SPFs used are sets of ortho-normalized harmonic oscillator functions in the mass-frequency scaled coordinates used. In the multiset formalism, one set is required for each particle for each electronic state. The initial wave function is the vibrational wave function of CP in its ground electronic state, which is simply

Jahn−Teller Interactions in Cyclopropane Radical Cation

J. Phys. Chem. A, Vol. 111, No. 10, 2007 **1751**

TABLE 2: Normal Mode Combinations and Sizes of the Primitive and the Single Particle Basis Used in the WP Propagation Using the MCTDH Algorithm on the (a) $\tilde{X}^2E'$ Electronic Manifold within the Linear Vibronic Coupling Scheme, (b) $\tilde{A}^2E''$ Electronic Manifold within the Quadratic Vibronic Coupling Scheme, and (c) $\tilde{X}^2E'−\tilde{A}^2E''$ Coupled Electronic Manifold within the Quadratic JT Plus Linear PJT Coupling Scheme[a]

normal modes[b]	primitive basis[c]	SPF basis[d]	CPU time	required RAM [Mbyte]	figure
		(a) $[E'_x, E'_y]$[d]			
(ν_1, ν_2, ν_3)	(8, 20, 3)	[8, 8]	E'_x: 13 h 41 min 12 s	234.6	4a
(ν_{4x}, ν_{4y})	(40, 40)	[30, 30]	E'_y: 13 h 28 min 21 s	234.6	
(ν_{5x}, ν_{5y})	(40, 40)	[30, 30]			
(ν_{6x}, ν_{6y})	(8, 8)	[10, 10]			
		(b) $[E''_x, E''_y]$[e]			
(ν_1, ν_2, ν_3)	(4, 21, 7)	[8, 8]	E''_x: 14 h 44 min 50 s	204.1	7d
(ν_{4x}, ν_{4y})	(23, 23)	[22, 22]	E''_y: 15 h 6 min 16 s	204.1	
(ν_{5x}, ν_{5y})	(6, 6)	[12, 12]			
(ν_{6x}, ν_{6y})	(22, 22)	[22, 22]			
(ν_{7x}, ν_{7y})	(8, 8)	[10, 10]			
		(c) $[E'_x, E'_y, E''_x, E''_y]$[f]			
(ν_1, ν_2, ν_3)	(7, 23, 9)	[10, 10, 5, 5]	E'_x: 126 h 15 min 26 s	972.5	8b
(ν_{4x}, ν_{4y})	(40, 40)	[22, 22, 17, 17]	E''_x: 136 h 3 min 2 s	972.5	
(ν_{5x}, ν_{5y})	(40, 40)	[22, 22, 16, 16]	E''_y: 82 h 14 min 32 s	972.5	
$(\nu_{6x}, \nu_{6y}, \nu_8)$	(12, 12, 19)	[14, 14, 15, 15]	E'_y: 116 h 31 min 2 s	972.5	
$(\nu_{7x}, \nu_{7y}, \nu_{9x}, \nu_{9y})$	(5, 5, 8, 8)	[13, 13, 11, 11]			

[a] The CPU time and the required memory of each run are also given. The calculations were converged with respect to the spectrum. [b] Vibrational modes bracketed together were treated as a single particle, e.g., particle 1 is a 3-dimensional particle including modes ν_1, ν_2, and ν_3. [c] The primitive basis is the number of harmonic oscillator DVR functions, in the dimensionless coordinate system required to represent the system dynamics along the relevant mode. Here we note that the numbers of basis functions are identical in both the time-independent (cf. Table 3) and time-dependent calculations. The primitive basis for each particle is the product of the one-dimensional bases; e.g., for particle 2 in Table 2a, the primitive basis was $40 \times 40 = 1600$ functions. The full primitive basis consists of a total of 7.86×10^{10} functions. [d] The SPF basis is the number of single-particle functions used, one set for each of the two electronic (component) states. Here they are the same in number to give equal weight for the x and y components of the degenerate $^2E'$ electronic state. The total number of configurations is 144 000. [e] The full primitive basis consists of a total of 3.46×10^{11} functions and there are 929 280 configurations altogether. [f] The full primitive basis consists of a total of 1.62×10^{16} functions and there are 2 210 560 configurations altogether.

expressed as a product of the first SPFs in each set and assumes the form of a Gaussian wave packet. The various mode combination schemes, the sizes of the primitive and SPF bases used in the present calculations are given in Table 2.

IV. Results and Discussion

A. Electronic Structure Calculations. For the detailed dynamical study, the various coupling parameters of the vibronic Hamiltonian of eqs 6a–6j, need to be determined first. We therefore perform detailed ab initio calculations of the electronic potential energy surfaces of the $\tilde{X}^2E'$ and $\tilde{A}^2E''$ electronic states of CP⁺ along the dimensionless normal coordinates of all 21 vibrational degrees of freedom. The important and most relevant vibrational modes are then selected and included in the dynamical calculations based on their coupling strength. The geometry optimization and the calculation of harmonic vibrational frequencies (ω_i) of CP in its ground electronic state ($\tilde{X}^1A_1'$) are carried out at the Møller−Plesset perturbation (MP2) level of theory employing the correlation-consistent polarized valence triple-ζ (cc-pVTZ) Gaussian basis set of Dunning.[40] The electronic structure calculations were performed using the Gaussian program package.[41] Along with the vibrational frequencies, the transformation matrix from the symmetry coordinates to the mass-weighted normal coordinates is obtained. The dimensionless normal coordinates (Q_i) are obtained by multiplying the latter with $\sqrt{\omega_i}$.[42] The vertical ionization energies of CP are calculated by the outer valence Green's function (OVGF) method[43,44] employing the same basis set. The resulting ionization energy values are equated with the adiabatic potential energies of the $\tilde{X}^2E'$ and $\tilde{A}^2E''$ electronic states of CP⁺. The calculations are carried out as a function of the dimensionless normal mode displacement coordinates $Q_i = -1.50$ (0.25), $+1.50$ using the Gaussian program package.[41]

The coupling parameters of the Hamiltonian represent derivatives of the adiabatic potential energy function of CP⁺ of appropriate order with respect to the dimensionless normal coordinates Q_i of the vibrational mode ν_i calculated at the equilibrium geometry of the neutral CP ($\mathbf{Q} = 0$). The linear and quadratic coupling parameters for the a_1' and e' vibrational modes are calculated by nonlinear least-square fits to the computed adiabatic energies of the $\tilde{X}^2E'$ and $\tilde{A}^2E''$ electronic states of CP⁺.

The $\tilde{X}E'−\tilde{A}^2E''$ PJT coupling parameters for the a_1'' and e'' vibrational modes can be obtained from

$$\lambda''_i = \frac{1}{2}\sqrt{\left(\frac{\partial^2 \Delta E}{\partial Q_i^2}\right)\Bigg|_{\mathbf{Q}=0}}, \qquad i = 8, 9 \qquad (18)$$

Here $\Delta E = \Delta V_{Q_i}^2 - \Delta V_0^2$, where $\Delta V_{Q_i}^2$ and ΔV_0^2 are the potential energy differences between the $\tilde{A}^2E''$ and $\tilde{X}^2E'$ electronic states for the normal mode displacement Q_i, and for the equilibrium configuration ($\mathbf{Q} = 0$), respectively. The PJT coupling parameters can be obtained by a suitable numerical finite difference scheme. The determination of the parameters through nonlinear least-square fits for the $\tilde{X}^2E'$ electronic states of CP⁺ is discussed in our previous article.[27] Similar fits are carried out for the $\tilde{A}^2E''$ electronic states to derive the corresponding parameters. For example, the vertical ionization potentials along the totally symmetric vibrational modes are fitted to extract κ'' and γ'', the mean of the JT split surfaces along the degenerate vibrational modes is fitted to extract γ'' along these modes and the signed differences of the JT split surfaces are fitted to obtain λ'' and η'' along the degenerate vibrational modes. For brevity we do not show these fits here, and the parameters derived from these fits are given in Table 1 along with the results for the $\tilde{X}^2E'$ ground electronic states,
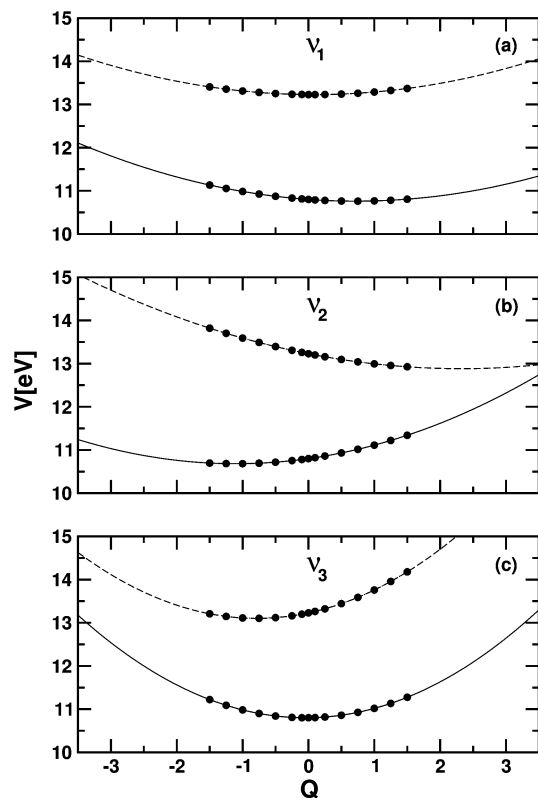
Figure 2. Adiabatic potential energy curves of the $\tilde{X}^2E'$ (solid lines) and $\tilde{A}^2E''$ (dashed lines) electronic states of CP$^+$ along the dimensionless normal coordinates for the totally symmetric (a_1'): (a) ν_1 (C–C stretching), (b) ν_2 (CH$_2$ scissoring), and (c) ν_3 (symmetric C–H stretching) vibrational modes. Each curve in the figure represents a cut along the multidimensional potential energy hypersurface of the respective electronic states. The equilibrium geometry of CP in its electronic ground state ($^1A_1'$) corresponds to $\mathbf{Q} = 0$. The ab initio ionization energies with a harmonic contribution from the neutral ground electronic state are shown by the filled circles on the diagram.

reproduced from ref 27 for completeness. We note that there was a typographical error for the γ and η values given in Table 2 of ref 27, which is corrected here. This error, however, does not affect the results presented in ref 27.

B. Adiabatic Potential Energy Surfaces. The adiabatic potential energy surfaces of the $\tilde{X}^2E'$ and $\tilde{A}^2E''$ electronic states

are obtained by diagonalizing the diabatic electronic Hamiltonian matrix given in eqs 3–6j. In the absence of the PJT coupling of the a_1'' and e'' vibrational modes, the eigenvalues of the $\tilde{X}^2E'$ and $\tilde{A}^2E''$ electronic states are given by

$$\mathcal{V}_{1,2}(\mathbf{Q}) = \mathcal{V}_0'(\mathbf{Q}) + E_{E'}^0 +$$
$$\sum_{i=1}^{3}\kappa_i'Q_i + \frac{1}{2}\sum_{i=1}^{3}\gamma_i'Q_i^2 + \frac{1}{2}\sum_{i=4}^{7}\gamma_i'(Q_{xi}^2 + Q_{yi}^2) \mp$$
$$\sqrt{\left[\sum_{i=4}^{7}\left(\lambda_i'Q_{xi} + \frac{1}{2}\eta_i'(Q_{xi}^2 - Q_{yi}^2)\right)\right]^2 + [\sum_{i=4}^{7}(\lambda_i'Q_{yi} - \eta_i'Q_{xi}Q_{yi})]^2}$$
$$(19a)$$

$$\mathcal{V}_{3,4}(\mathbf{Q}) = \mathcal{V}_0'(\mathbf{Q}) + E_{E''}^0 +$$
$$\sum_{i=1}^{3}\kappa_i''Q_i + \frac{1}{2}\sum_{i=1}^{3}\gamma_i''Q_i^2 + \frac{1}{2}\sum_{i=4}^{7}\gamma_i''(Q_{xi}^2 + Q_{yi}^2) \mp$$
$$\sqrt{\left[\sum_{i=4}^{7}\left(\lambda_i''Q_{xi} + \frac{1}{2}\eta_i''(Q_{xi}^2 - Q_{yi}^2)\right)\right]^2 + [\sum_{i=4}^{7}(\lambda_i''Q_{yi} - \eta_i''Q_{xi}Q_{yi})]^2}$$
$$(19b)$$

where $\mathcal{V}_1'$ and $\mathcal{V}_2'$ refer to the lower and upper adiabatic sheets of the $\tilde{X}^2E'$ electronic manifold and $\mathcal{V}_3'$ and $\mathcal{V}_4'$ to the lower and upper adiabatic sheets of the $\tilde{A}^2E''$ electronic manifold, respectively. With the aid of the parameters of Table 1, the adiabatic potential energy surfaces of the quadratic vibronic model are obtained. In Figure 2a–c, we show one-dimensional cuts of these multidimensional potential energy hypersurfaces along the totally symmetric vibrational modes ν_1, ν_2, and ν_3. In the figure the potential energy values obtained from the above quadratic vibronic model are shown by the solid and dashed lines for the $\tilde{X}^2E'$ and $\tilde{A}^2E''$ electronic states, respectively, and the corresponding ab initio computed energies are superimposed on them and indicated by the filled circles. The electronic degeneracy of these states is restored upon displacements along the symmetric vibrational modes. It can be seen that the model reproduces the computed energies very well.

One-dimensional cuts of the above two electronic states along the x-component of the JT active vibrational modes ν_4, ν_5, ν_6, and ν_7 are plotted in Figure 3a–d. As above, the solid and
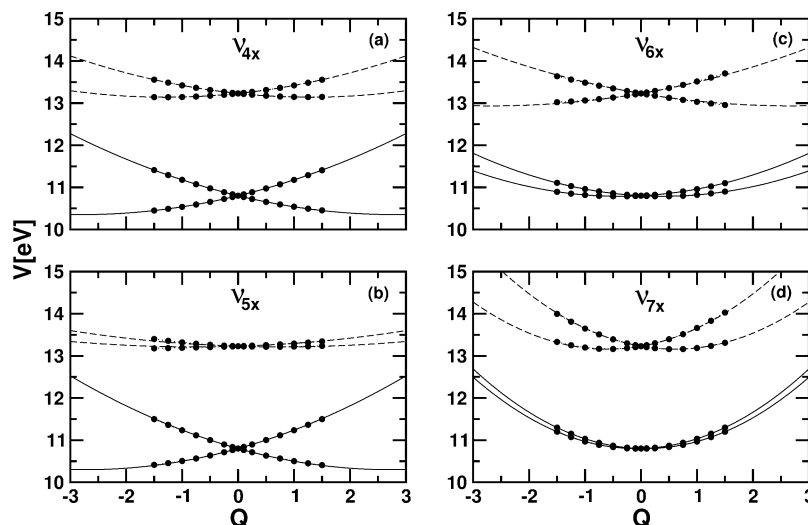

Figure 3. Adiabatic potential energy curves of the JT split $\tilde{X}^2E'$ (solid lines) and the $\tilde{A}^2E''$ (dashed lines) electronic states of CP$^+$ plotted as a function of the x component of the dimensionless normal coordinates of the degenerate (e'): (a) ν_4 (CH$_2$ wagging mode), (b) ν_5 (ring deformation), (c) ν_6 (CH$_2$ scissoring), and (d) ν_7 (asymmetric C–H stretching) vibrational modes. The ab initio ionization energies with a harmonic contribution from the neutral ground electronic state are shown by the filled circles on the diagram.

Jahn−Teller Interactions in Cyclopropane Radical Cation

J. Phys. Chem. A, Vol. 111, No. 10, 2007 **1753**

dashed lines describe the energy values obtained from the model for the $\tilde{X}^2E'$ and $\tilde{A}^2E''$ electronic states, respectively, and the points superimposed on them represent the corresponding computed energies. It can be seen that the degeneracy of the $\tilde{X}^2E'$ and $\tilde{A}^2E''$ electronic states is split upon displacements along these modes. It is noteworthy that the degenerate vibrational modes ν_4 and ν_5 cause a large JT splitting in the $\tilde{X}^2E'$ electronic manifold compared to that in the $\tilde{A}^2E''$ electronic manifold. On the other hand, the vibrational modes ν_6 and ν_7 cause a relatively large splitting of the degeneracy of the $\tilde{A}^2E''$ electronic manifold when compared to that of the $\tilde{X}^2E'$ electronic manifold. It is apparent from Figure 3 that the JT coupling in the $\tilde{X}^2E'$ electronic manifold is stronger than in the $\tilde{A}^2E''$ electronic manifold, which is also revealed by the magnitude of the coupling strengths given in Table 1. We note that the cuts of the $\tilde{X}^2E'$ electronic manifold are reproduced here from ref 27 for completeness. The curve crossings at the origin in the above figures represent the conical intersections associated with the $(E \times e)$-JT effect. In addition, there are curve crossings between the upper sheet of the $\tilde{X}^2E'$ and the lower sheet of the $\tilde{A}^2E''$ electronic states, which will be shown and discussed below.

At this point it is useful to examine a few stationary points of the potential energy surfaces discussed above. In our previous article,[27] we have already discussed the stationary points of the $(E \times e)$-JT PESs of the $\tilde{X}^2E'$ electronic manifold. In the following, we consider the $(E \times e)$-JT PESs of the $\tilde{A}^2E''$ electronic manifold and also its PJT coupling with the $\tilde{X}^2E'$ electronic manifold. In the space of a_1' vibrational modes, the minimum of the seam of conical intersections now occurs at Q_i^0 $(i = 1-3) = -\kappa_i''/(\omega_i + \gamma_i'')$, and the energy at the minimum is given by

$$\mathscr{V}_{\min,\text{JT}}^{(c)} = E_{E''}^0 - \frac{1}{2}\sum_{i=1}^{3}\frac{\kappa_i''^2}{(\omega_i + \gamma_i'')} \quad (20)$$

When distorted along the JT active e' vibrational modes, this energetic minimum changes to a cusp and new minima and saddle points appear on the lower adiabatic component of the JT split $\tilde{A}^2E''$ electronic manifold. Along one component (e.g., x) of these doubly degenerate vibrational modes, two solutions are obtained for $Q_{xi} = \mp\lambda_i''/(\omega_i + \gamma_i'' \pm \eta_i'')$ $(i = 4-7)$, with energies

$$\mathscr{V}_{-}^0 = E_{E''}^0 - \frac{1}{2}\sum_{i=1}^{3}\frac{\kappa_i''^2}{(\omega_i + \gamma_i'')} - \frac{1}{2}\sum_{i=4}^{7}\frac{\lambda_i''^2}{(\omega_i + \gamma_i'' - \eta_i'')} \quad (21)$$

and

$$\mathscr{V}_{-}^{\text{sp}} = E_{E''}^0 - \frac{1}{2}\sum_{i=1}^{3}\frac{\kappa_i''^2}{(\omega_i + \gamma_i'')} - \frac{1}{2}\sum_{i=4}^{7}\frac{\lambda_i''^2}{(\omega_i + \gamma_i'' + \eta_i'')} \quad (22)$$

where $\mathscr{V}_{-}^0$ and $\mathscr{V}_{-}^{\text{sp}}$ refer to the energy of the new minima and the saddle points, respectively. Using the parameters given in Table 1, we obtain $\mathscr{V}_{\min,\text{JT}}^{(c)} = 12.756$ eV occurring at $Q_1^0 = 0.085$, $Q_2^0 = 2.320$, and $Q_3^0 = -0.784$; $\mathscr{V}_{-}^0 = 12.118$ eV occurring at $Q_{4x}^0 = 1.266$, $Q_{5x}^0 = 0.668$, $Q_{6x}^0 = 4.155$, and $Q_{7x}^0 = 0.668$; and $\mathscr{V}_{-}^{\text{sp}} = 12.374$ eV occurring at $Q_{4x}^{\text{sp}} = -1.327$, $Q_{5x}^{\text{sp}} = -0.904$, $Q_{6x}^{\text{sp}} = -1.822$, and $Q_{4x}^{\text{sp}} = -0.587$ for the $\tilde{A}^2E''$ electronic manifold. The JT stabilization energy of the latter

amounts to ∼0.638 eV. A similar analysis revealed a higher JT stabilization energy of ∼0.986 eV for the $\tilde{X}^2E'$ electronic manifold.[27]

We now provide an approximate estimate of the energetic minimum of the PJT crossings of the $\tilde{X}^2E'$ and $\tilde{A}^2E''$ electronic states. We repeat that the PJT active modes here are of a_1'' and e'' symmetry, and only two such modes, ν_8 (a_1'') and ν_9 (e''), are relevant in the present situation. Defining $\Sigma = (E_{E'}^0 + E_{E''}^0)/2$, $\Delta = (E_{E''}^0 - E_{E'}^0)/2$, $\sigma_i = (\kappa_i' + \kappa_i'')/2$, $\delta_i = (\kappa_i'' - \kappa_i')/2$, $\sigma_i' = (\lambda_i' + \lambda_i'')/2$, $\delta_i' = (\lambda_i'' - \lambda_i')/2$ and setting Q_{yi}, Q_8, Q_{9x}, $Q_{9y} = 0$, the energetic minimum of the seam of conical intersections between the JT split components of the $\tilde{X}^2E'$ and $\tilde{A}^2E''$ electronic states occurs at[7]

$$\mathscr{V}_{\min,\text{PJT}}^{(c)} = \Sigma + \frac{(F - \Delta)^2}{2D} - \frac{1}{2}\sum_{i=1}^{3}\frac{\sigma_i^2}{\omega_i} - \frac{1}{2}\sum_{i=4}^{7}\frac{\sigma_i'^2}{\omega_i} \quad (23)$$

where

$$F = \sum_{i=1}^{3}\frac{\delta_i\sigma_i}{\omega_i} + \sum_{i=4}^{7}\frac{\delta_i'\sigma_i'}{\omega_i} \quad (24)$$

$$D = \sum_{i=1}^{3}\frac{\delta_i^2}{\omega_i} + \sum_{i=4}^{7}\frac{\delta_i'^2}{\omega_i} \quad (25)$$

At this point it is necessary to discuss a few technical points. The determination of the energetic minimum of the PJT crossing using eq 23 requires the knowledge of a definite relative sign of the JT coupling parameters λ_i' and λ_i'' in the $\tilde{X}^2E'$ and $\tilde{A}^2E''$ electronic states, respectively. In principle, there may be four different possibilities for this relative sign: (i) $\lambda_i' > 0$, $\lambda_i'' > 0$; (ii) $\lambda_i' > 0$, $\lambda_i'' < 0$; (iii) $\lambda_i' < 0$, $\lambda_i'' < 0$; (iv) $\lambda_i' < 0$, $\lambda_i'' > 0$. The last two possibilities do not yield any new results when compared to the first two. Using the parameters given in Table 1 one finds that $\mathscr{V}_{\min,\text{PJT}}^{(c)}$ occurs at 12.878 eV in case i and at 12.118 eV in case ii. The first value is ∼0.123 eV above and the second one is ∼0.638 eV below the minimum of the JT conical intersections in the $\tilde{A}^2E''$ electronic manifold. In practice, the relative signs of these two JT parameters is fixed by examining the invariance property of the Hamiltonian matrix with respect to the symmetry operations of the D_{3h} point group. Such an exercise is detailed in the Appendix. This shows that (ii) is the correct option in this case. Therefore, the minimum of the PJT crossing in the present situation occurs ∼1.475 eV above the minimum of the $\tilde{X}^2E'$ and ∼0.638 eV below the minimum of the $\tilde{A}^2E''$ JT conical intersections in CP$^+$.

C. Photoelectron Spectrum. In this section we report on the photoelectron bands revealing the vibronic energy level structure of the $\tilde{X}^2E'$ and $\tilde{A}^2E''$ electronic states of CP$^+$. These photoelectron bands are calculated by the time-independent and time-dependent quantum mechanical methods described above and using the parameters of Table 1. Consistencies of various theoretical results are explicitly checked whenever possible, and the final theoretical results are compared with the experimental data.[20] The final theoretical results of this paper are, however, obtained by propagating wave packets using the MCTDH algorithm.[28−30] In the following, we start with various reduced dimensional models and systematically approach the full simulation of nuclear dynamics using the four states and fourteen modes Hamiltonian of eqs 6a−6j.

1. $\tilde{X}^2E'$ Photoelectron Band. In our previous article,[27] we have described the calculation of this photoelectron band in detail

1754 *J. Phys. Chem. A, Vol. 111, No. 10, 2007*
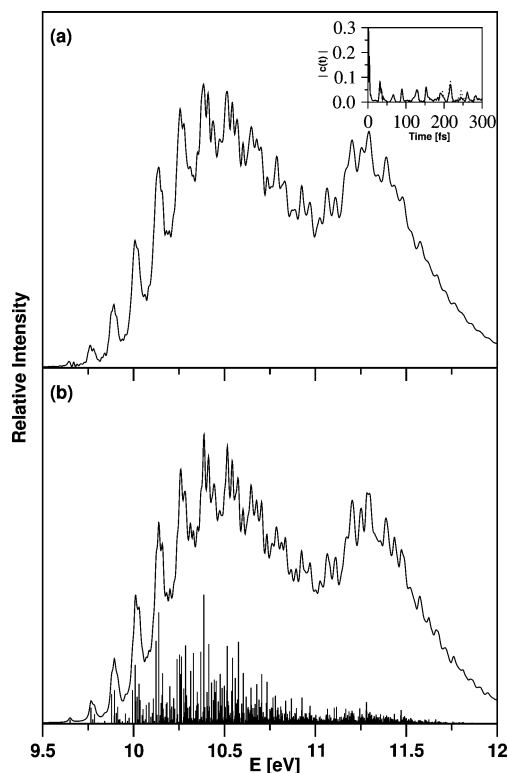
Venkatesan et al.

Figure 4. First photoelectron band of CP revealing the vibronic level structure of the $\tilde{X}^2E'$ electronic manifold of CP$^+$. The intensity (in arbitrary units) is plotted as a function of the energy of the final vibronic state. The energy is measured relative to the zero-point level of the electronic ground state of CP. The photoelectron band obtained by the wave packet propagation method within the MCTDH scheme considering a two-state six-mode model is shown in panel a. The absolute values of the time autocorrelation functions $|C(t)|$ computed by locating the initial wave packet separately on the two component states of the $\tilde{X}^2E'$ electronic manifold are plotted in the inset of panel a and are shown by the solid and dotted lines. The corresponding results obtained by the time-independent matrix diagonalization method are essentially reproduced from ref 27 (see text) and shown in panel b.

by the time-independent quantum mechanical approach discussed above. To optimize various numerical parameters in the time-dependent WP calculations using the MCTDH scheme, we in the following simulate this band once again using the Hamiltonian developed in the previous paper[27] and compare the time-independent and time-dependent results. In the time-dependent simulations, the linear vibronic Hamiltonian for the $\tilde{X}^2E'$ electronic manifold is used considering the three totally symmetric Condon active (ν_1, ν_2 and ν_3) and three degenerate JT active (ν_4, ν_5 and ν_6) vibrational modes as in ref 27. These modes are found to be primarily important, and form the major progressions in the vibronic structure of the $\tilde{X}^2E'$ photoelectron band. The combination of normal modes, the sizes of the primitive and SPF bases used for these calculations are given in the upper part of Table 2. A total of four multidimensional particles are used: Of these, particle 1 is three-dimensional and combines ν_1, ν_2, and ν_3 vibrational modes. The remaining three particles are two-dimensional and combine the x and y components of ν_4, ν_5, and ν_6 vibrational modes, respectively. The sizes of the primitive and SPF bases are selected in such a way that the calculations are converged with respect to the vibronic structure of the photoelectron band.

The photoelectron band thus obtained is shown in Figure 4a along with the corresponding time-independent results in Figure 4b. The latter is essentially reproduced from Figure 7b of ref 27. Note a slight difference in the spectral intensity distribution

of Figure 4a and Figure 7b of ref 27 beyond ~11.70 eV. This is because of an intensity cutoff used in the convolution procedure underlying the earlier Figure 7b. This leads to an artificial reduction in the spectral intensity for high energy. The theoretical spectrum in panel *a* represents a sum of contributions from the two JT split components (x and y) of the degenerate $\tilde{X}^2E'$ electronic manifold. Each of these contributions is the Fourier transform of the time-autocorrelation function $C^m(t)$ computed with an initial WP located on the mth electronic state (cf. eq 13). The WP in each calculation is propagated for 150 fs, which effectively yields $C^m(t)$ up to 300 fs, using the prescription, $C^m(t) = \langle \Psi^m(t/2)^* | \Psi^m(t/2) \rangle$, for a real initial WP.[45] This prescription helps to increase the energy resolution, $\Delta E = 2\pi\hbar/T$, in the spectrum by effectively doubling the propagation time T. A constant energy shift of -0.743 eV was applied while plotting the photoelectron band in Figure 4a to match the energy ranges covered by the time-independent "stick" spectrum (cf. Figure 4b). This, in turn, reproduces the adiabatic ionization position of the band at its experimental value along the abscissa.[27] The overall width and the tiny structures of both the spectral envelopes are in very good agreement with each other over the entire energy range. The splitting between the two maxima in the bimodal intensity distribution in Figure 4a is ~0.81 eV and compares well with the time-independent (cf. Figure 4b) and experimental results of ~0.80 eV and ~0.78 eV, respectively.

To account for the finite broadening of the experimental spectra due to poor energy resolution of the spectrometer and also due to the possible role of additional degrees of freedom (like rotation) not considered here, the stick vibronic spectrum is convoluted with a suitable line-shape function of appropriate width. In the time-dependent picture, the latter is equivalent to damping the autocorrelation function by a time-dependent function. By a careful choice of this function, one can minimize the artifacts due to the finite length of propagation time. In the following, all spectra resulting from the time-dependent calculations are obtained by damping the corresponding autocorrelation functions by the time-dependent function

$$F(t) = \cos\left(\frac{\pi t}{2T}\right) \tag{26}$$

with T being the total length of the time propagation. As $t \rightarrow T$, $F(t) C(t) \rightarrow 0$ and therefore the artifacts due to finite time Fourier transformation are reduced. Multiplying $C(t)$ with $F(t)$ is equivalent to convoluting the spectrum with the Fourier transform of $F(t)$, which in this case reads[31]

$$\tilde{F}(\omega) = \frac{4\pi T}{\pi^2 - (2\omega T)^2} \cos(\omega T) \tag{27}$$

with a fwhm of $\Gamma = 3.4/T$. Further phenomenological broadening, due to the spectral resolution and neglect of the other degrees of freedom, is added by the function

$$G(t) = \exp\left(\frac{-t}{\tau_r}\right) \tag{28}$$

with τ_r being the relaxation time. This leads to a Lorentzian broadening of the spectrum with fwhm $\Gamma = 2/\tau_r$. In Figure 4a the vibronic spectrum of the $\tilde{X}^2E'$ electronic manifold is obtained by damping the autocorrelation function with $\tau_r = 66$ fs ($\Gamma \approx 20$ meV).

2. $\tilde{A}^2E''$ Photoelectron Band. To unravel the complex vibronic structure of the second photoelectron band of CP, we here treat
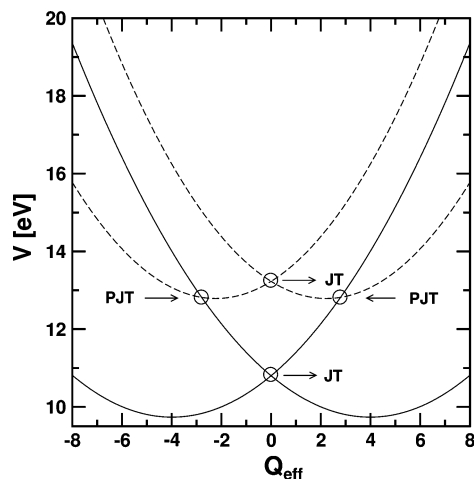
Figure 5. Schematic drawing of the JT and PJT conical intersections in the $\tilde{X}E'-\tilde{A}^2E''$ coupled electronic manifold of CP. The potential energies of the JT split components of the $\tilde{X}^2E'$ (solid lines) and $\tilde{A}^2E''$ (dashed lines) are plotted along the dimensionless normal coordinate of an effective vibrational mode (see text for further details). They appear as curve crossings and are marked by open circles in the diagram.

the nuclear dynamics systematically in the isolated $\tilde{A}^2E''$ electronic manifold first and then finally for the coupled $\tilde{X}E'-\tilde{A}^2E''$ electronic states of CP$^+$. The second photoelectron band at ∼13 eV, attributed to the vibronic structure of $\tilde{A}^2E''$ electronic manifold of CP$^+$, is essentially structureless (cf. Figure 1). To reveal the coupling effects of various vibrational modes on the vibronic fine structure of this band, we first examine the nuclear dynamics by employing the linear and the quadratic coupling scheme, separately in the $\tilde{A}^2E''$ electronic manifold alone. For this purpose we used the time-independent matrix diagonalization scheme to solve the eigenvalue equation (cf. eq 14) to find the precise locations of the vibronic energy levels. The simulation of the nuclear dynamics in the coupled $\tilde{X}E'-\tilde{A}^2E''$ electronic states is more involved and computationally unfeasible with the matrix diagonalization approach and is therefore carried out by the WP propagation approach using the MCTDH scheme.

It is mentioned in section I that the $\tilde{X}^2E'$ and $\tilde{A}^2E''$ electronic states can couple together via the PJT active a_1'' and e'' vibrational modes. The minimum of the seam of PJT crossings occurs below/above the minimum of the JT conical intersections in the $\tilde{A}^2E''/\tilde{X}^2E'$ electronic states. The intersections of JT split components of the $\tilde{X}E'-\tilde{A}^2E''$ electronic manifold are schematically shown in Figure 5. In this drawing, the potential energies of these component electronic states are plotted as a function of the dimensionless normal coordinates of an effective vibrational mode. The latter is constructed individually for the $\tilde{X}^2E'$ and $\tilde{A}^2E''$ electronic states by combining the highly excited a_1' and e' vibrational modes in those states. From Table 1 it can be seen that the coupling strengths of the ν_2, ν_4, and ν_5 vibrational modes in the $\tilde{X}^2E'$ electronic manifold and that of the ν_2, ν_4, and ν_6 vibrational modes in the $\tilde{A}^2E''$ electronic manifold are significant. Therefore, the mentioned vibrational modes are considered within the respective electronic states and the effective first-order coupling constant, $\kappa_{\text{eff}} = \sqrt{\sum_i \kappa_i^2}$, and effective vibrational frequency, $\omega_{\text{eff}} = \sum_i \omega_i \kappa_i^2 / \kappa_{\text{eff}}^2$, for the effective mode are calculated. Therefore, in the schematic diagram of Figure 5, the effective mode for the $\tilde{X}^2E'$ electronic manifold consists of ν_2, ν_4, and ν_5 and that for the $\tilde{A}^2E''$ electronic manifold consists of ν_2, ν_4, and ν_6 vibrational modes. The crossings of the PESs in Figure 5, become multidimensional conical intersections in the multidimensional space of a_1' and e' vibrational modes. Therefore, a WP initially excited to one
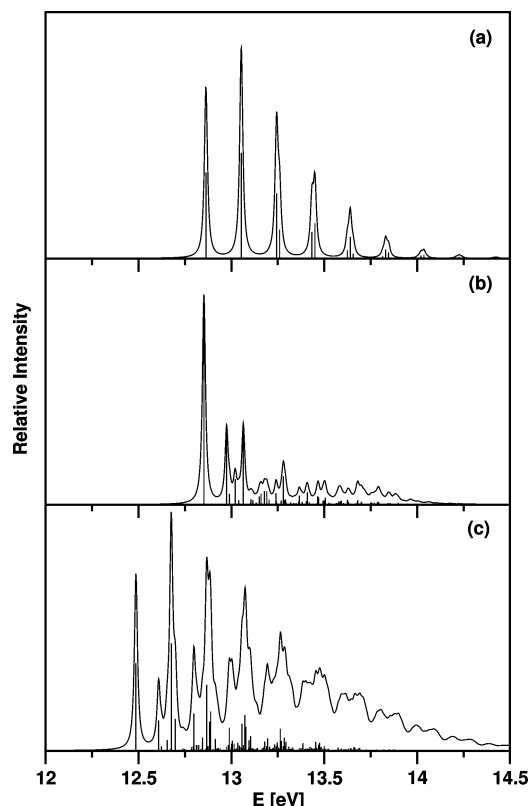

Figure 6. Second photoelectron band of CP pertaining to an ionization to the $\tilde{A}^2E''$ electronic manifold of CP$^+$ calculated within the linear vibronic coupling scheme: (a) partial spectrum obtained with the three symmetric a_1' vibrational modes $\nu_1-\nu_3$, (b) partial spectrum obtained with the four JT active degenerate e' vibrational modes $\nu_4-\nu_7$, and (c) the composite theoretical spectrum obtained by convoluting the above two partial spectra. The stick vibronic spectrum of each panel is convoluted with a Lorentzian function of 20 meV fwhm to generate the spectral envelope.

component of the $\tilde{A}^2E''$ electronic manifold would approach these multiple multidimensional conical intersections and the resulting nuclear motion is expected to be highly nonadiabatic. In the following, we save some space to discuss this nonadiabatic transition of the nuclear WP to the component electronic states of the $\tilde{X}E'-\tilde{A}^2E''$ electronic manifold by examining the time evolution of a WP initially prepared on the $\tilde{A}^2E''$ electronic manifold.

The $\tilde{A}^2E''$ photoelectron band is calculated with the linear and also the quadratic vibronic coupling scheme in the absence of the PJT coupling with the $\tilde{X}^2E'$ electronic manifold. In the absence of any intermode bilinear coupling terms, the Hamiltonian is decoupled in terms of the a_1' and e' vibrational modes. In the numerical calculations we take advantage of this property and calculate two partial spectra by considering the a_1' and e' vibrational modes separately in the nuclear dynamics. Finally, these two partial spectra are convoluted together to generate the composite full spectrum. This property of the Hamiltonian substantially reduces the computational overheads by effectively reducing the dimension of the secular matrix for each calculation.

In Figure 6a the partial spectrum obtained with the three totally symmetric a_1' vibrational modes ν_1, ν_2, and ν_3 within the linear vibronic coupling scheme is shown. The spectral intensity in arbitrary units is plotted as a function of the energy of the final vibronic state. The stick eigenvalue spectrum is convoluted with a Lorentzian line shape function of 20 meV fwhm to generate the spectral envelope. The same Lorentzian function

TABLE 3: Number of Harmonic Oscillator (HO) Basis Functions along Each Vibrational Mode, the Dimension of the Secular Matrix, and the Number of Lanczos Iterations Used To Calculate the Converged Theoretical Stick Spectrum Shown in Various Figures Noted Below

no. of HO basis functions							dimension of the secular matrix	no. of Lanczos iterations	figure
ν_1	ν_2	ν_3	ν_4	ν_5	ν_6	ν_7			
8	20	3					960	1500	4b
			40	40	8		33 359 445	15 000	4b
4	38	10					3040	1500	6a, 7a
			23	2	22	5	51 207 200	15 000	6b, 7b

is used to convolute all time-independent stick spectra shown below. In Table 3, the number of harmonic oscillator basis functions along the considered vibrational modes, the size of the secular matrix and the number of Lanczos iterations used in computing the numerically converged spectra are given.

The spectrum in Figure 6a reveals dominant excitation of the ν_2 vibrational mode. The excitation of the ν_3 vibrational mode is weaker. The vibrational mode ν_1 on the other hand does not reveal any noticeable excitation. Relatively strong excitation of the ν_2 vibrational mode compared to that for ν_1 and ν_3 was also observed in the $\tilde{X}^2E'$ photoelectron band.[27] However, ν_1 is the weakest mode in the $\tilde{A}^2E''$ electronic manifold in contrast to ν_3 in the $\tilde{X}^2E'$ electronic manifold. The peaks in the spectrum in Figure 6a are $\sim$190 meV and $\sim$396 meV spaced in energy and correspond to the frequency of the ν_2 and ν_3 vibrational modes, respectively.

The spectrum obtained with the JT active vibrational modes ν_4, ν_5, ν_6 and ν_7 within the linear coupling scheme is shown in Figure 6b. A convolution of the symmetric mode spectrum of Figure 6a and the JT spectrum of Figure 6b is presented in Figure 6c. The JT spectrum in Figure 6b reveals dominant excitation of the ν_4 and ν_6 vibrational modes. The excitation strength of these two vibrational modes are almost the same (cf. Table 1). Peak spacings of $\sim$122, $\sim$137, $\sim$187, and $\sim$397 meV can be observed in the spectrum and they correlate with the frequencies of the ν_4, ν_5, ν_6, and ν_7 vibrational modes, respectively. The excitation of the ν_5 and ν_7 vibrational modes, however, is much weaker compared to that for ν_4 and ν_6. We note that the JT coupling strengths of the e' vibrational modes in the $\tilde{A}^2E''$ electronic manifold are much weaker compared to those in the $\tilde{X}^2E'$ electronic manifold. The JT coupling of the ν_4 and ν_5 vibrational modes in the latter electronic manifold is quite strong, and therefore, a distinct bimodal intensity distribution is observed for the first photoelectron band of CP. The dominant excitations in the convoluted composite spectrum of Figure 6c are therefore due to the ν_2, ν_3, ν_4, and ν_6 vibrational modes. When compared with the case for the experimental band shown in Figure 1, it can be seen that the linear coupling approach is not at all adequate to reproduce the highly diffuse structure of the second photoelectron band of CP.

The effect of the second-order coupling terms of the Hamiltonian on the vibronic structure of the above photoelectron band is shown in Figure 7a–c. The number of harmonic oscillator functions for each vibrational mode, size of the secular matrix, and the number of Lanczos iterations required to obtain numerically converged stick spectra in Figure 7a–c are given in Table 3. The two partial spectra computed separately with the a_1' and e' vibrational modes are shown in panels a and b, respectively, and a convolution of the two is shown in panel c. In comparison with the linear coupling spectra of Figure 6a–c, the second-order coupling terms, in general, cause an increase of the spectral line density. The dominant progression in the
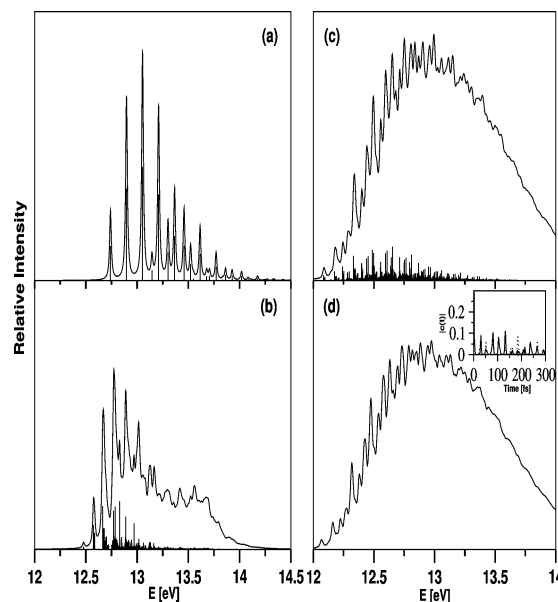

Figure 7. Panels a–c: same as in Figure 6a–c, obtained with the quadratic vibronic coupling model. Panel d: results obtained by the wave packet propagation method within the MCTDH scheme, using the same quadratic vibronic Hamiltonian for the $\tilde{A}^2E''$ electronic manifold as employed above. The absolute value of the time autocorrelation function, $|C(t)|$, computed by locating the initial wave packet separately on the two component states of this degenerate electronic manifold is shown by the solid and dotted lines in the inset.

composite spectrum of Figure 7c is mainly caused by the ν_2, ν_4, and ν_6 vibrational modes. It can be seen that the quadratic JT coupling terms significantly increase the spectral line density and, as a result, the spectral envelope becomes broad and diffuse and it resembles more closely the experimental envelope (cf. Figure 1) when compared to the linear coupling results (cf. Figure 6c and Figure 7c). In Figure 7d the same photoelectron band is shown as obtained by propagating wave packets within the MCTDH scheme. The spectrum in Figure 7d is obtained by combining two partial spectra calculated by locating the initial WP on the x and y component of the $\tilde{A}^2E''$ electronic manifold separately. The time dependence of the autocorrelation function, $|C(t)|$, for these two initial conditions are shown as an inset in Figure 7d, by the solid and dotted lines. The details of the mode combinations and the size of various bases used in the WP propagation are given in Table 2. It can be seen from the inset of Figure 7d that the time period of the quasi-periodic oscillations in $|C(t)|$ remains the same; however, their amplitude differs for the two initial conditions. The damping time (66 fs) of the autocorrelation function in Figure 7d corresponds to the convolution width (20 meV fwhm Lorentzian function) of the spectrum in Figure 7c. The vibronic fine structure of the time-dependent spectrum of panel d is virtually in perfect accord with the time-independent results of panel c.

3. Final $\tilde{X}^2E'-\tilde{A}^2E''$ Photoelectron Band. So far we did not include the PJT coupling due to the a_1'' and e'' vibrational modes in the calculations. When these coupling terms are considered in the Hamiltonian, the separability of the Hamiltonian in terms of the symmetric and degenerate vibrational modes as explored above no longer exists. It is therefore necessary to simulate the nuclear dynamics on four component electronic states of the coupled $\tilde{X}E'-\tilde{A}^2E''$ electronic manifold simultaneously including all relevant vibrational degrees of freedom. As mentioned before, this task is computationally impractical by the time-independent matrix diagonalization approach.
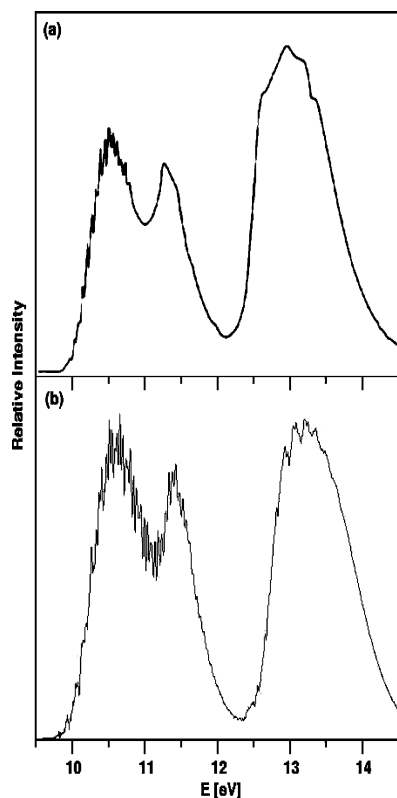
Jahn−Teller Interactions in Cyclopropane Radical Cation

J. Phys. Chem. A, Vol. 111, No. 10, 2007 **1757**

Figure 8. Photoelectron bands (first and second) of CP. The final theoretical results are shown in panel b along with the experimental results of Holland and co-workers[20] in panel a. The relative intensity in arbitrary units is plotted as a function of the energy of the vibronic levels of the $\tilde{X}E'-\tilde{A}^2E''$ coupled electronic manifold. The zero of energy corresponds to the zero-point energy of the electronic ground state of CP. The theoretical results are obtained by the WP propagation approach using the MCTDH algorithm (see text).

The complete photoelectron band that represents the final results of this paper is therefore simulated by propagating wave packets using the MCTDH program package,[28] including four electronic states and fourteen relevant vibrational degrees of freedom. Four WP propagations are carried out separately by locating the initial WP on each of the component electronic states of the coupled $\tilde{X}E'-\tilde{A}^2E''$ electronic manifold. The fourteen vibrational degrees of freedom are grouped into five particles, out of which one is four dimensional, two are three-dimensional, and the remaining two are two-dimensional. The detailed combination scheme of the vibrational modes is given in Table 2 along with the sizes of the primitive and SPF bases. These parameters are optimally chosen to ensure the numerical convergence of the photoelectron band. The WP for each initial location is propagated for 150 fs, which leads to ~13.7 meV energy resolution in the photoelectron band. The final theoretical results are shown in panel b of Figure 8 along with the experimental results in panel a. The final theoretical spectrum of panel b represents a combination of the partial spectra obtained for four different initial conditions stated above. The relative intensity in arbitrary units is plotted as a function of the energy of the final vibronic state. It can be seen from Figure 8 that the theoretical results compare extremely well with the experiment. We note that to generate the partial spectra the autocorrelation functions are damped with $\tau_r = 66$ fs (≈ 20 meV) before Fourier transformation.

The theoretical results in Figure 8b when compared with the results of Figure 7c,d discussed above immediately reveal the strong impact of the PJT coupling on the vibronic structure of both the photoelectron bands. The vibronic structure of the
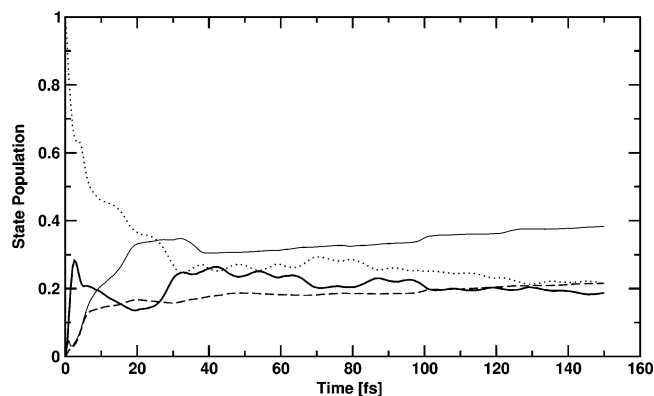

Figure 9. Time evolution of the diabatic electronic populations obtained by locating an initial wave packet on one component of the $\tilde{A}^2E''$ electronic manifold of CP$^+$. The decay of the population of this component electronic state is shown by the dotted line and the growth of the population of the other component of the $\tilde{A}^2E''$ electronic state and the two JT split components of the $\tilde{X}^2E'$ electronic state is shown by the thick solid line, solid and dashed lines, respectively.

second band is perturbed starting from its origin. This is because the minimum of the seam of PJT conical intersections occurs ~0.638 eV below that of the $\tilde{A}^2E''$ JT conical intersections. The PJT coupling of the two degenerate electronic states causes a huge increase in spectral line density−the almost continuum levels of the $\tilde{X}^2E'$ electronic manifold mix with the low-lying vibronic levels of the $\tilde{A}^2E''$ electronic manifold. This mixing of levels of two different vibronic symmetries causes the increase in the spectral line density. As a result, the second maximum due to the JT split upper adiabatic cone of the $\tilde{X}^2E'$ electronic manifold of the first photoelectron band and the entire second photoelectron band becomes moderately and extremely diffuse and structureless, respectively. Despite a good overall agreement between theory and experiment, there are remaining minor discrepancies in the finer details of the two. For example, the overall widths of the second maximum of the first band and the second band are somewhat narrow compared to the experimental results. These minor discrepancies may be attributed to the inadequate energy resolution in the experimental recording and also to the neglect of the intermode coupling terms of the Hamiltonian in the theoretical calculations. The impact of the latter on the vibronic structure of the photoelectron band is presently being examined and will be discussed in a forthcoming publication.

D. Time-Dependent Wave Packet Dynamics. In this section we discuss the femtosecond internal conversion dynamics of a WP initially prepared on one component of the JT split $\tilde{A}^2E''$ electronic manifold. This WP during its evolution in time approaches all the JT and PJT conical intersections in the $\tilde{X}E'-\tilde{A}^2E''$ coupled electronic manifold (shown schematically in Figure 5), and nonradiatively transits to all four component electronic states of this manifold. The time dependence of the diabatic electronic populations of these four electronic states is shown in Figure 9. The WP is initially located on one component of the $\tilde{A}^2E''$ electronic manifold. The population of this state starts from 1.0 at $t = 0$ and decays to a value of ~0.20 at longer times (dotted line). The initial decay of population of this state relates to a decay rate of ~10 fs. Companion calculations reveal a decay rate of ~10 fs of the second component of the $\tilde{A}^2E''$ electronic manifold. It can be seen from Figure 9 that at $t = 0$ the population of the remaining three electronic states of the $\tilde{X}E'-\tilde{A}^2E''$ electronic manifold is zero. At longer times the WP approaches the PJT and JT conical intersections and undergoes nonadiabatic transitions and populates these three electronic

states. The population of the second component of the $\tilde{A}^2E''$ electronic manifold and that of the x and y components of the $\tilde{A}^2E'$ electronic manifold is shown in Figure 9 by the thick solid line, solid line, and dashed line, respectively. Finally, the populations of both the components of the $\tilde{A}^2E''$ electronic manifold saturate nearly to the same value. When the WP is initially prepared on the JT split component of the $\tilde{X}^2E'$ electronic manifold, the population transfer to the $\tilde{A}^2E''$ electronic manifold is found to be negligible (diagram not shown here). This WP moves back and forth between the two component electronic states only through the $\tilde{X}^2E'$ JT conical intersections and their populations fluctuate around an average value of $\sim$0.5.

To better understand the population dynamics of Figure 9, in Figure 10a−f we show snapshots of the WP evolving on the $\tilde{X}E'$−$\tilde{A}^2E''$ coupled electronic manifold. The probability density ($|\Psi|^2$) of the WP is superimposed on the potential energy curves along the normal coordinate of the strongest Condon active a_1' vibrational mode ν_2. The potential energy curves and the WP probability densities are shown as solid and dashed lines for the $\tilde{X}^2E'$ and $^2E''$ electronic states, respectively. For the purpose of drawing, the zero of the WP probability densities is chosen to occur near a potential energy of $\sim$13.5 eV. Because the Condon activity of ν_2 is strongest in both the electronic states, most of the significant structures in the population diagram of Figure 9 can be interpreted from the WP snapshots along this mode. Again we mention that the electronic degeneracy of the two electronic states is retained along this totally symmetric vibrational mode.

Because the WP is initially (at $t = 0$) located on one component of the $\tilde{A}^2E''$ electronic manifold (not shown in the figure), the population of this state starts from 1.0 (dotted line in Figure 9). In about 5 fs (cf. Figure 10a), a fraction of population ($\sim$42%) transfers to the $\tilde{X}^2E'$ electronic manifold and as a result a sharp drop in the $\tilde{A}^2E''$ population occurs (cf. Figure 9). In about 10 fs (Figure 10b), the WP component on the $\tilde{A}^2E''$ electronic manifold moves more toward the $\tilde{X}$−$\tilde{A}$ PJT crossing seam, and in $\sim$40 fs (Figure 10d), it moves solely toward it. At longer times (Figure 10e,f), the remaining WP component on this electronic manifold moves closer to its potential energy minimum. The WP component on the $\tilde{X}^2E'$ electronic manifold, on the other hand, moves away from the crossing seam and mostly remains localized near its "own" potential energy minimum. This is because the minimum of the $\tilde{X}E'$−$\tilde{A}^2E''$ PJT crossing seam occurs $\sim$1.475 eV above the minimum of the $\tilde{X}^2E'$ electronic manifold. Therefore, the recrossing probability of the WP component on this electronic manifold to the $\tilde{A}^2E''$ electronic manifold is expected to be very small. We note that in addition to this crossing through the $\tilde{X}$−$\tilde{A}$ PJT conical intersections, the WP component on each degenerate electronic manifold undergoes crossing through the respective JT conical intersections. The seam of the latter occurs at the equilibrium configuration $\mathbf{Q} = 0$. Therefore, motion of the WP toward the minimum of the potential energy curves in Figure 10 is associated with the population exchange between the JT split components of the respective degenerate electronic manifold. This is revealed by the growth of population in time of the three JT component states in Figure 9. The weak structures in the population diagram appear due to the interference of the WP components in the vicinity of various curve crossings in the $\tilde{X}E'$−$\tilde{A}^2E''$ coupled electronic manifold.

V. Summary and Outlook

A detailed theoretical description of the multimode JT and PJT interactions in the low-lying doubly degenerate $\tilde{X}^2E'$ and
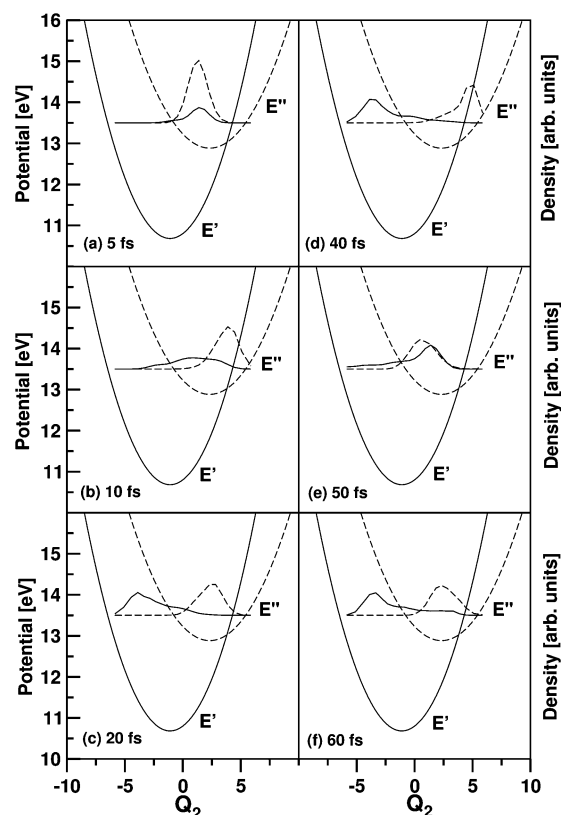

Figure 10. Wave packet probability densities ($|\Psi|^2$) as a function of the dimensionless normal coordinate Q_2 of the vibrational mode ν_2 integrated over all other coordinates at different times (indicated in each panel) superimposed on the potential energy curves of the $\tilde{A}^2E''$ (dashed line) and $\tilde{X}^2E'$ (solid line) electronic states of CP$^+$. The WP probability densities on these electronic states are shown by the same line types. The zero of the WP probability densities has been chosen, for graphical reasons, to occur near a potential energy of 13.5 eV. The scales for the probability density are arbitrary but identical for all $|\Psi|^2$ displayed in the figure.

$\tilde{A}^2E''$ electronic states of CP$^+$ has been presented. Degenerate vibrational modes of e' symmetry split the electronic degeneracy of these electronic states and the resulting JT split component states exhibit PJT interactions via the vibrational modes of a_1'' and e'' symmetry. The theoretical model here is constructed by considering interactions among these four component electronic states and fourteen relevant vibrational degrees of freedom. Quantum dynamical simulations of the nuclear motion are carried out both by a time-independent and by a time-dependent approach and the vibronic level structure of this coupled manifold of electronic states is calculated. The theoretical results are compared with the available experimental photoelectron spectrum of CP.

In the theoretical description, a model vibronic Hamiltonian of the four interacting electronic states including the fourteen vibrational degrees of freedom is constructed in terms of the dimensionless normal coordinates of the electronic ground state of CP in a diabatic electronic basis. A quadratic vibronic coupling scheme is employed to describe the Condon activity of the three a_1' vibrational modes and the JT activity of the four e' vibrational modes. The PJT activity of the a_1'' and e'' vibrational modes is treated by a linear vibronic coupling scheme. The coupling parameters of the Hamiltonian are determined by calculating the adiabatic potential energy surfaces of the $\tilde{X}^2E'$ and $\tilde{A}^2E''$ electronic states along each vibrational mode by the OVGF method.

TABLE 4: Characters and Transformation Matrices of Basis Functions of the D_{3h} Irreducible Representations for Some Symmetry Operations of the C_{3v} Subgroup

	A_1'	A_2'	E'	A_1''	A_2''	E''
E	1	1	$\begin{pmatrix} 1 & 0 \\ 0 & 1 \end{pmatrix}$	1	1	$\begin{pmatrix} 1 & 0 \\ 0 & 1 \end{pmatrix}$
C_3	1	1	$\begin{pmatrix} -\frac{1}{2} & -\frac{\sqrt{3}}{2} \\ \frac{\sqrt{3}}{2} & -\frac{1}{2} \end{pmatrix}$	1	1	$\begin{pmatrix} -\frac{1}{2} & -\frac{\sqrt{3}}{2} \\ \frac{\sqrt{3}}{2} & -\frac{1}{2} \end{pmatrix}$
σ_v	1	−1	$\begin{pmatrix} -1 & 0 \\ 0 & 1 \end{pmatrix}$	−1	1	$\begin{pmatrix} -1 & 0 \\ 0 & 1 \end{pmatrix}$

In the nuclear dynamical simulations, we systematically examined the vibronic energy level structure of the $\tilde{X}^2E'$ and $\tilde{A}^2E''$ electronic states of CP$^+$ first by considering the JT interactions alone in both these states and then by introducing the PJT interactions between the two. To start with, we reproduced the time-independent results on the first band shown in ref 27 by the time-dependent WP propagation method employed here. The $\tilde{A}^2E''$ photoelectron band is then calculated by considering three Condon active ($\nu_1-\nu_3$) and four JT active vibrational modes ($\nu_4-\nu_7$) within a linear coupling scheme by the time-independent method. The results obtained from this linear coupling approach do not correspond well with the experiment. The effect of the second-order coupling terms of the Hamiltonian is then considered and the spectrum is calculated by both the time-independent and time-dependent approaches. The second-order coupling terms cause an increase in the spectral line density, and the spectral envelope reveals much better agreement with the experiment. The dominant progression in this band is mainly caused by the ν_2, ν_4, and ν_6 vibrational modes. The vibronic fine structure of the time-dependent spectrum of Figure 7d is in very good accord with the time-independent one of Figure 7c.

The complete photoelectron band that represents the final result of this paper is simulated by propagating wave packets using the MCTDH approach, including four electronic states and fourteen relevant vibrational degrees of freedom. Such a task is computationally not viable by the time-independent matrix diagonalization approach. When we compare the theoretical results with the experimental one, a strong impact of the PJT coupling on the vibronic structure of both the photoelectron bands can be observed. The impact of the PJT coupling on the second band is more than that on the first band. This is because the minimum of the seam of PJT conical intersections occurs ~0.638 eV below that of the $\tilde{A}^2E''$ JT conical intersections. As a result, the continuum levels of the $\tilde{X}^2E'$ electronic manifold mix with the low-lying vibronic levels of the $\tilde{A}^2E''$ electronic manifold. The huge increase in the spectral line density results from this mixing of levels of two different vibronic symmetries. Despite a good overall agreement between theory and experiment, there are minor discrepancies in the finer details of the two. More precisely, the overall width of the second maximum of the first band and that of the second band are somewhat narrow compared to the experimental findings. These minor discrepancies may be attributed to the inadequate energy resolution in the experimental recording and also to the neglect of the various bilinear coupling terms (a$_1'$-a$_1'$, a$_1'$-e$'$ and e$'$-e$'$) of the Hamiltonian in the theoretical calculations. An analysis of the latter on the vibronic structure of the photoelectron band is presently underway and will be discussed in a forthcoming publication.

The time evolution of the diabatic electronic populations reveals a nonradiative decay time of ~10 fs of the $\tilde{A}^2E''$ electronic manifold of CP$^+$ mediated by the PJT interaction with the $\tilde{X}^2E'$ electronic manifold through the a$''$ and e$''$ vibrational modes. The $\tilde{X}E'-\tilde{A}^2E''$ photoelectron band of CP$^+$ represents a unique and complex example of the interplay between the JT and PJT interactions involving two doubly degenerate electronic states treated here for the first time.

Appendix

In this Appendix we demonstrate the correctness of the Hamiltonian matrix, eqs 3−6j, that is, show that the various coupling terms transform totally symmetric under the symmetry operations of the pertinent point group, D_{3h}. The general reasoning is similar to the one developed for the benzene radical cation in the appendix of ref 46. Only linear coupling terms will be considered here; quadratic coupling terms can be treated in an analogous way.

To simplify the analysis, we note that the proper transformation behavior under the reflection operation σ_h is already ensured by the superscripts (primes) embodied in the symmetry selection rules, eqs 1 and 2, and the Hamiltonian matrix elements of eqs 3−6j. We can confine the analysis, therefore, to a suitable subgroup of D_{3h}, which we choose to be C_{3v} and thus have identical representation matrices for the E' and E'' electronic states (as well as for e$'$ and e$''$ vibrational modes). These are given in Table 4, which focuses on only one convenient choice for the C_3 and σ_v symmetry operations.

With the underlying phase conventions, one arrives at the following transformation properties of the electronic projection operators in the E' as well as E'' electronic function spaces (because the superscripts are not needed, the kets $|x\rangle$ and $|y\rangle$, as well as the corresponding bras, refer collectively to the first and second rows/columns of the E' as well as E'' representation matrices of the Table 4).

$$|x\rangle\langle y| - |y\rangle\langle x| \xrightarrow{C_3} |x\rangle\langle y| - |y\rangle\langle x| \tag{A1}$$

$$|x\rangle\langle y| - |y\rangle\langle x| \xrightarrow{\sigma_v} - (|x\rangle\langle y| - |y\rangle\langle x|) \tag{A2}$$

$$\begin{pmatrix} |x\rangle\langle x| - |y\rangle\langle y| \\ |x\rangle\langle y| + |y\rangle\langle x| \end{pmatrix} \xrightarrow{C_3} \begin{pmatrix} -1/2 & \sqrt{3}/2 \\ -\sqrt{3}/2 & -1/2 \end{pmatrix} \begin{pmatrix} |x\rangle\langle x| - |y\rangle\langle y| \\ |x\rangle\langle y| + |y\rangle\langle x| \end{pmatrix} \tag{A3}$$

$$\begin{pmatrix} |x\rangle\langle x| - |y\rangle\langle y| \\ |x\rangle\langle y| + |y\rangle\langle x| \end{pmatrix} \xrightarrow{\sigma_v} \begin{pmatrix} 1 & 0 \\ 0 & -1 \end{pmatrix} \begin{pmatrix} |x\rangle\langle x| - |y\rangle\langle y| \\ |x\rangle\langle y| + |y\rangle\langle x| \end{pmatrix} \tag{A4}$$

Note that the latter two relations hold only for the specific transformation matrices given in Table 4.

Let us denote by Q_x and Q_y the nuclear displacement coordinates transforming as the $|y\rangle$ and $|x\rangle$ electronic basis states,

respectively. Then, transformation laws similar to eqs A3−A4 hold for them also, and one can subsequently verify that the operator

$$\mathbf{W}_e = (Q_x, Q_y)\begin{pmatrix} |x\rangle\langle x| - |y\rangle\langle y| \\ |x\rangle\langle y| + |y\rangle\langle x| \end{pmatrix} \tag{A5}$$

remains invariant under the C_3 and σ_v symmetry operations, i.e., transforms totally symmetric in the C_{3v} molecular point group. Because the additional symmetry operations of D_{3h} need no further consideration (see second paragraph of the Appendix), this establishes the correctness of all coupling terms linear in the coordinates of the e' and e'' modes in eqs 6a−6j. One notes that they have all (including the PJT coupling terms) the usual forms familiar from JT theory.

We next investigate the coupling terms involving nondegenerate vibrational modes. The labeling of their vibrational coordinates follows the same indexing convention as the irreducible representations according to which they transform. Then, within an electronic state, there are only the following two totally symmetric electron-vibrational operators (cf. the Table 4 and eqs A1 and A2):

$$\mathbf{W}_{a_1'} = Q_1'(|x\rangle\langle x| + |y\rangle\langle y|) \tag{A6}$$

$$\mathbf{W}_{a_2'} = Q_2'(|x\rangle\langle y| - |y\rangle\langle x|) \tag{A7}$$

Equations A6 and A7 hold again for the E' as well as for the E'' state. Equation A6 reproduces (for completeness) the well-known results about the linear coupling to totally symmetric modes, whereas eq A7, does not satisfy the requirement of hermiticity and the corresponding coupling element has to be dropped in the Hamiltonian (for a corresponding momentum coupling operator, however, see ref 47).

Concerning the PJT coupling terms, the E' and E'' electronic basis states now have to be distinguished by corresponding superscripts. Then, eqs A1 and A2 and the Table 4 allow us to see rather easily that the following two (and only two) electron-vibrational operators transform totally symmetric (that is, are form-invariant under the C_3 and σ_v symmetry operations):

$$\mathbf{W}_{a_1''} = Q_1''(|x'\rangle\langle y''| - |y'\rangle\langle x''|) \tag{A8}$$

$$\mathbf{W}_{a_2''} = Q_2''(|x'\rangle\langle x''| + |y'\rangle\langle y''|) \tag{A9}$$

Note that the vibrational subscripts 1 and 2 are interchanged as compared to those in eqs A6 and A7. This is a direct consequence of the different transformation properties of, e.g., Q_1' and Q_1'' according to Table 4. Also, the PJT coupling term (A8) does *not* violate hermiticity because it appears in the off-diagonal 2×2 blocks of the 4×4 coupling matrix, eq 3. Taken together, in matrix form the relations (A6)−(A9) establish the linear coupling terms also for the nondegenerate vibrational modes in eqs 6a−6j. Here the element $\mathbf{W}_{a_2''}$ from eq A9 is suppressed because these modes turn out to be unimportant for CP^+.

We point out that the form of $\mathbf{W}_{a_1''}$ of eq A8 may be changed by a suitable redefinition of either the E' or the E'' electronic basis states. This, however, would lead to different $E \otimes e$ JT coupling matrices in these states and underlines that care is needed to work with a consistent choice of electronic wave functions to arrive at correct Hamiltonians for simultaneous JT and PJT interactions.

It remains to clarify the determination of the relative signs of the JT coupling constants λ' and λ'' for the various modes.

These prove to be important (at least for the a_1'' coupling mode) for reasons similar to those discussed earlier for the benzene radical cation.[32] They can be determined, e.g., by using symmetry-adapted displacements of the JT active modes. In the higher-symmetry subgroup of D_{3h} (here C_{2v}) the two JT-split potential energy surfaces are then distinguished by symmetry and can be identified with either of the diagonal elements of the coupling matrix of eqs 3−6j. (Thus λ' and λ'' are signed quantities.)

Lacking symmetry-adapted JT displacements we may perform electronic structure calculations for simultaneous JT and PJT displacements and deduce the relative signs of λ' and λ'' (for a given mode) from the repulsion pattern of the potential energy surfaces. This is seen by transforming the Hamiltonian eqs 3−6j to an electronic basis that is adiabatic *within* each of the E' and E'' electronic states only (resulting in an interaction matrix $\mathbf{W}^{tr}$). For a single JT-mode displacement this is achieved by the same 2×2 orthogonal matrix (in either degenerate state), which leaves the Q_1'' coupling term invariant according to the following result:

$$\mathbf{W}^{tr} = \begin{pmatrix} \lambda'\rho & 0 & 0 & \lambda Q_1'' \\ 0 & -\lambda'\rho & -\lambda Q_1'' & 0 \\ 0 & -\lambda Q_1'' & \lambda''\rho & 0 \\ \lambda Q_1'' & 0 & 0 & -\lambda''\rho \end{pmatrix} \tag{A10}$$

Here ρ is the polar radius for the JT active mode in question, and the λ' and λ'' are signed quantities. Equation A10 demonstrates that for the same sign of λ' and λ'' the PJT mode Q_1'' couples the upper with the lower sheet of the E' and E'' electronic manifolds, whereas for opposite signs it couples the upper sheets with each other (and also the lower ones, of course). This allows us to determine the relative signs, provided the displacements are chosen suitably to reveal the difference between the two cases.

References and Notes

(1) Jahn, H. A.; Teller, E. *Proc. R. Soc. London Ser. A* **1937**, *161*, 220.

(2) Öpik, U.; Pryce, M. H. L. *Proc. R. Soc. London, Ser. A* **1957**, *238*, 425. Longuet-Higgins, H. C.; Öpik, U.; Pryce, M. H. L.; Sack, R. A. *Proc. R. Soc. A* **1958**, *244*, 1. Longuet-Higgins, H. C. *Adv. Spectrosc.* **1961**, *2*, 429.

(3) Englman, R. *The Jahn-Teller Effect in Molecules and Crystals*; Wiley: New York, 1972.

(4) Bersuker, I. B.; Polinger, V. Z. *Vibronic Interactions in molecules and crystals*; Springer-Verlag: Berlin, 1989.

(5) Bersuker, I. B. *Chem. Rev.* **2001**, *101*, 1067.

(6) *Conical Intersections: Electronic Structure, Dynamics and Spectroscopy*; Domcke, W., Yarkony, D. R., Köppel, H., Eds.; World Scientific: Singapore, 2004.

(7) Köppel, H.; Domcke, W.; Cederbaum, L. S. *Adv. Chem. Phys.* **1984**, *57*, 59.

(8) Teller, E. *J. Phys. Chem.* **1937**, *41*, 109. Herzberg G.; Longuet-Higgins, H. C. *Discuss. Faraday Soc.* **1963**, *35*, 77. Carrington, T. *Discuss. Faraday Soc.* **1972**, *53*, 27. Yarkony, D. R. *Rev. Mod. Phys.* **1996**, *68*, 985. Yarkony, D. R. *Acc. Chem. Res.* **1998**, *31*, 511. Robb, M. A. *Pure Appl. Chem.* **1995**, *67*, 783. Bernardi, F.; Olivucci, M.; Robb, M. A. *Chem. Soc. Rev.* **1996**, *25*, 321. Conical intersections in photochemistry, spectroscopy and chemical dynamics. *Chem. Phys.* **2000**, *259*, 121−337.

(9) Robb, M. A. *Reviews in Computational Chemistry*; Lipkowitz, K., Boyd, D., Eds.; Wiley: New York, 2000; Vol. 15, p 87.

(10) *The Role of Degenerate States in Chemistry*; Baer, M., Billing, G. D., Eds.; Advances in Chemistry and Physics Vol. 124; Wiley: Hoboken, NJ, 2002.

(11) Barckholtz, T. A.; Miller, T. A. *Int. Rev. Phys. Chem.* **1998**, *17*, 435.

(12) Born, M.; Oppenheimer, R. *Ann. Phys. (Leipzig)* **1927**, *84*, 457.

(13) Born M.; Huang, K. *The Dynamical Theory of Crystal Lattices*; Oxford University Press: Oxford, U.K., 1954.

(14) Cederbaum, L. S. In *Conical Intersections: Electronic Structure, Dynamics and Spectroscopy*; Domcke, W., Yarkony, D. R., Köppel, H., Eds.; World Scientific: Singapore, 2004; pp 3−40. Worth, G. A.; Cederbaum, L. S. *Ann. Rev. Phys. Chem.* **2004**, *55*, 127.

(15) Perrin, M. H.; Gouterman, M. *J. Chem. Phys.* **1967**, *46*, 1019. van der Waals, J. H.; Berghuis, A. M. D.; de Groot, M. S. *Mol. Phys.* **1967**, *13*, 301. ibid. **1971**, *21*, 497. Stephens, P. J. *J. Chem. Phys.* **1969**, *51*, 1995.

(16) Zgierski, M. Z.; Pawlikowski, M. *J. Chem. Phys.* **1979**, *70*, 3444.

(17) Köppel, H.; Cederbaum, L. S.; Domcke, W. *J. Chem. Phys.* **1988**, *89*, 2023.

(18) Turner, D. W.; Baker, C.; Baker, A. D.; Brundle, C. R. *Molecular Photoelectron Spectroscopy*; Wiley: New York, 1970.

(19) Kimura, K.; Katsumata, S.; Achiba, Y.; Yamazaki, T.; Iwata, S. *Handbook of HeI Photoelectron Spectra of Fundamental Organic Molecules*; Japan Scientific Societies Press: 1981.

(20) Holland, D. M. P.; Karlsson, L.; Siegbahn, K. *J. Electron Spectrosc. Relat. Phenom.* **2002**, *125*, 57.

(21) Leng, F. J.; Nyberg, G. L. *J. Electron Spectrosc. Relat. Phenom.* **1977**, *11*, 293.

(22) Basch, H.; Robin, M. B.; Kuebler, N. A.; Baker, C.; Turner, D. W. *J. Chem. Phys.* **1969**, *51*, 52.

(23) Schweig, A.; Thiel, W. *Chem. Phys. Lett.* **1973**, *21*, 541.

(24) Lindholm, E.; Fridh, C.; Åsbrink, L. *Faraday Discuss. Chem. Soc.* **1972**, *54*, 127.

(25) Potts, A. W.; Streets, D. G. *J. Chem. Soc., Faraday Trans. 2* **1974**, *70*, 875.

(26) Keller, P. R.; Taylor, J. W.; Carlson, T. A.; Whitley, T. A.; Grimm, F. A. *Chem. Phys.* **1985**, *99*, 317.

(27) Venkatesan, T. S.; Mahapatra, S.; Cederbaum, L. S.; Köppel, H. *J. Phys. Chem. A* **2004**, *108*, 2256.

(28) Worth, G. A.; Beck, M. H.; Jäckle, Meyer, H.-D. The MCTDH Package, Version 8.2, University of Heidelberg, Germany, 2000. Meyer, H.-D.; Version 8.3, 2002. See http://www.pci.uni-heidelberg.de/tc/usr/mctdh/

(29) Meyer, H.-D.; Manthe, U.; Cederbaum, L. S. *Chem. Phys. Lett.* **1990**, *165*, 73.

(30) Manthe, U.; Meyer, H.-D.; Cederbaum, L. S. *J. Chem. Phys.* **1992**, *97*, 3199.

(31) Beck, M. H.; Jäckle, A.; Worth, G. A.; Meyer, H.-D. *Phys. Rep.* **2000**, *324*, 1.

(32) Köppel, H.; Döscher, M.; Baldea, I.; Meyer, H.-D.; Szalay P. G. *J. Chem. Phys.* **2002**, *117*, 2657.

(33) Markmann, A.; Worth, G. A.; Mahapatra, S.; Meyer, H.-D.; Köppel, H.; Cederbaum, L. S. *J. Chem. Phys.* **2005**, *123*, 204310.

(34) Lichten, W. *Phys. Rev.* **1967**, *164*, 131. Smith, F. T. *Phys. Rev.* **1969**, *179*, 111. O'Malley, T. F. *Adv. At. Mol. Phys.* **1971**, *7*, 223. Pacher, T.; Cederbaum, L. S.; Köppel, H. *Adv. Chem. Phys.* **1993**, *84*, 293.

(35) Domcke, W.; Köppel, H.; Cederbaum, L. S. *Mol. Phys.* **1981**, *43*, 851.

(36) Cullum, J.; Willoughby, R. *Lanczos Algorithms for Large Symmetric Eigenvalue Problems*; Birkhäuser: Boston, 1985; Vols. I and II.

(37) Köppel, H.; Domcke, W. In *Encyclopedia of Computational Chemistry*; P. v. R. Schleyer, Ed.; Wiley: New York, 1998; p 3166.

(38) Dirac, P. A. M. *Proc. Cambridge Philos. Soc.* **1930**, *26*, 376.

(39) Frenkel, J. *Wave Mechanics*; Clarendon: Oxford, U.K., 1934.

(40) Dunning, T. H., Jr. *J. Chem. Phys.* **1989**, *90*, 1007.

(41) Frisch, M. J.; Trucks, G. W.; Schlegel, H. B.; Gill, P. M. W.; Johnson, B. G.; Robb, M. A.; Cheeseman, J. R.; Keith, T.; Peterson, G. A.; Montgomery, J. A.; Raghavachari, K.; Al-Laham, M. A.; Zakrzewski, V. G.; Ortiz, J. V.; Foresman, J. B.; Cioslowski, J.; Stefanov, B. B.; Nanayakkara, A.; Challacombe, M.; Peng, C. Y.; Ayala, P. Y.; Chen, W.; Wong, M. W.; Andres, J. L.; Replogel, E. S.; Gomperts, R.; Martin, R. L.; Fox, D. J.; Binkley, J. S.; Defrees, D. J.; Baker, J.; Stewart, J. P.; Head-Gordon, M.; Gonzales, C.; Pople, J. A. *Gaussian* 98, revision E.1; Gaussian, Inc.: Pittsburgh, PA, 1995.

(42) Wilson, E. B., Jr.; Decius, J. C.; Cross, P. C. *Molecular Vibrations*; McGraw-Hill: New York, 1955.

(43) Cederbaum, L. S. *J. Phys. B* **1975**, *8*, 290.

(44) von Niessen, W.; Schirmer, J.; Cederbaum, L. S. *Comput. Phys. Rep.* **1984**, *1*, 57.

(45) Engel, V. *Chem. Phys. Lett.* **1992**, *189*, 76.

(46) Döscher, M.; Köppel, H.; Szalay, P. G. *J. Chem. Phys.* **2002**, *117*, 2645.

(47) Fletcher, J. R. *J. Phys. C: Solid State Phys.* **1981**, *14*, L491.